Analysis of ozone loss in the Arctic stratosphere during the late winter and spring of 1997 using the Chemical Species Mapping on Trajectories (CSMT) technique

Akiko Kagawa[1] and Sachiko Hayashida
Faculty of Science, Nara Women's University, Nara, Japan

Received 5 August 2002; revised 25 May 2003; accepted 14 July 2003; published 21 November 2003.

[1] A scheme to create synoptic maps of stratospheric minor species from asynoptic satellite measurements using a photochemical box model and trajectory analysis was developed and named Chemical Species Mapping on Trajectories (CSMT). CSMT combined with Improved Limb Atmospheric Spectrometer (ILAS) data were used to study the Arctic ozone loss mechanism in the late winter and early spring of 1997. Long- and short-lived species in the stratosphere were successfully mapped by the CSMT initialized with ILAS-observed ozone, nitric acid, and nitrous oxide. Comparisons of CSMT-derived data and ozonesonde data, and/or other satellite data, validated the scheme. The comparisons showed the reliability of the scheme in mapping long- and short-lived species. A chemical ozone loss amount was estimated using the chemical model; the maximum ozone loss rate was about 34 ppbv/day in late February. The integrated ozone loss from 13 January to 31 March was 41%, averaged over the entire polar vortex. The effects of differences in polar stratospheric cloud composition and a possible warm bias in the temperature data set were examined, and only minor differences were found in the ozone loss amount. The derived ozone loss rates and integrated ozone loss are consistent with results from other studies. The Arctic ozone loss in the late winter and early spring of 1997 depended significantly on latitude and showed complex features: ozone loss occurred mainly at lower latitudes until late February; the region of significant ozone loss shifted to higher latitudes in March. The CSMT scheme shows good potential for various applications including detailed analyses of chemical mechanisms in the atmosphere. *INDEX TERMS:* 0340 Atmospheric Composition and Structure: Middle atmosphere—composition and chemistry; 0341 Atmospheric Composition and Structure: Middle atmosphere—constituent transport and chemistry (3334); 3337 Meteorology and Atmospheric Dynamics: Numerical modeling and data assimilation; 3349 Meteorology and Atmospheric Dynamics: Polar meteorology; 9315 Information Related to Geographic Region: Arctic region; *KEYWORDS:* Arctic ozone loss, model, data assimilation

Citation: Kagawa, A., and S. Hayashida, Analysis of ozone loss in the Arctic stratosphere during the late winter and spring of 1997 using the Chemical Species Mapping on Trajectories (CSMT) technique, *J. Geophys. Res.*, *108*(D22), 4698, doi:10.1029/2002JD002824, 2003.

1. Introduction

[2] In the Arctic stratosphere, substantial ozone loss has been observed in late winter and early spring over the past decade [*World Meteorological Organization* (*WMO*), 1999]. Loss mechanisms are similar to those of the Antarctic ozone loss. Because Arctic dynamics are more complicated, however, the ozone loss evolves in a different manner. For example because the Arctic vortex is smaller and more distorted than the Antarctic vortex, Arctic air can be exposed to sunlight, even during the polar night. Furthermore, there is significant interannual variability in the spatial distribution of Arctic ozone. Because of the more complex dynamics in the Arctic vortex, separation of chemical ozone loss is more important over the Arctic, and several sophisticated methods have recently been developed to differentiate dynamical effects from observed ozone changes. One method considers the relationship between ozone and inert tracers, such as N_2O, to quantify the chemical ozone loss [e.g., *Manney et al.*, 1994]. Another (the "Match" technique [e.g., *Rex et al.*, 1999]) derives chemical ozone loss from a pair of balloon soundings that measure ozone in the same air parcel at different points on the same trajectory. Observed chemical ozone loss has been confirmed by these methods.

[3] Many models have been developed to investigate polar ozone loss [e.g., *Brasseur et al.*, 1997; *Portmann et al.*, 1996]. Chemical-transport models (CTM) are powerful tools for studying polar ozone loss, and have advanced the scientific understanding of Arctic ozone loss [*Chipperfield and Pyle*, 1998; *Guirlet et al.*, 2000; *Hansen and Chipperfield*,

[1]Now at Fujitsu FIP Corporation, Tokyo, Japan.

0148-0227/03/2002JD002824$09.00

1999; *Lefevre et al.*, 1998]. CTMs are computationally expensive, however. For local comparisons in a limited area, a box model that is integrated along trajectories is preferred. *Becker et al.* [1998, 2000] compared the ozone loss derived from a Match analysis to that estimated from a chemical box model along the same trajectory in the Arctic winter and spring of 1992 and 1995. Model calculations for January underestimated ozone loss, while those for February and March agreed with Match analysis. The inconsistency of ozone loss suggested an important unresolved issue in polar ozone chemistry [*Becker et al.*, 1998, 2000].

[4] A significant ozone reduction occurred over the Arctic in the late winter and early spring of 1997, a year that was marked by the presence of a polar vortex into early spring [*Newman et al.*, 1997]. In 1996/1997, temperatures did not fall to PSC formation temperatures (~195 K) until early January, which is relatively late as compared to other years. However, temperatures remained low through the end of March and a strong and symmetric vortex persisted into early May [*Coy et al.*, 1997]. Significant Arctic ozone loss was noted in 1997 by observations and models [*Chipperfield and Pyle*, 1998; *Guirlet et al.*, 2000; *Knudsen et al.*, 1998; *Hansen and Chipperfield*, 1999; *Newman et al.*, 1997; *Lefevre et al.*, 1998; *Manney et al.*, 1997; *Müller et al.*, 1997; *Sinnhuber et al.*, 1998; *Schulz et al.*, 2000; *Terao et al.*, 2002].

[5] The Improved Limb Atmospheric Spectrometer (ILAS) instrument developed by the Environmental Agency of Japan (EA) on board the Advanced Earth Observing Satellite (ADEOS) was launched in August 1996, and successfully observed ozone and ozone-related species such as HNO_3, NO_2, N_2O, H_2O, CH_4 and aerosols during this same winter [*Sasano et al.*, 1999]. ILAS was a solar occultation sensor with an infrared spectrometer, and provided vertical profiles of chemical species with 1-km height intervals. ILAS measured more than 6000 occultation events in the Northern and Southern Hemisphere from November 1996 to June 1997. ILAS observed 14 circumpolar points in each hemisphere daily at high latitudes (57.1–72.2°N and 64.3–88.2°S). An advantage of the ILAS measurements is that many minor chemical species can be observed simultaneously, allowing a detailed investigation of ozone loss mechanisms. Analysis of ILAS ozone data by *Terao et al.* [2002] showed a maximum chemical ozone loss of 50–80 ppbv/day in late February between θ = 400 K and θ = 600 K. This ozone loss correlates well with the appearance of ILAS-derived PSCs, as reported by *Sasano et al.* [2000] and *Hayashida et al.* [2000a], suggesting chlorine activation by heterogeneous reactions on the PSCs. Analysis of ILAS HNO_3 revealed large-scale denitrification after late February [*Kondo et al.*, 2000; *Irie et al.*, 2001], and *Pan et al.* [2002] reported a significant dehydration, which may have altered the chemical conditions under which chemical ozone loss occurred.

[6] In this study, synoptic maps of ozone loss were constructed based on results from a chemical box model and trajectory analysis, using ILAS measurements of minor species as initial conditions. Chemical mechanisms of ozone destruction in the late winter and early spring of 1997 were investigated based on the synoptic maps.

[7] Several schemes have been developed to address the difficulties of creating synoptic maps from asynoptically gathered trace gas data. These methods include the Kalman filter [*Haggard et al.*, 1986], the Salby-Fourier technique [*Salby*, 1982a, 1982b], and constituent reconstruction [*Schoeberl et al.*, 1989]. *Pierce et al.* [1994] used meteorological information to create synoptic maps. *Morris et al.* [1995, 2000] developed "Trajectory Mapping," which creates synoptic maps from asynoptic satellite data by advecting fields backward or forward in time on an analyzed field. Trajectory mapping has successfully made synoptic maps of long-lived minor constituents.

[8] Here we incorporated a chemical box model into trajectory mapping to estimate chemical change in the concentration of real-time chemical species. The scheme was named "Chemical Species Mapping on Trajectories (CSMT)." Chemical species from satellite measurement points are time-integrated toward a target time along trajectories that start at different times, and a synoptic map of chemical species is obtained. The CSMT is a useful method to understand the behavior of minor species, especially where complicated chemical/dynamical processes evolve, as in the Arctic because spatial distributions of long- and short-lived chemical species can be described on a global scale. In addition, the CSMT scheme can expand the area of geographically limited data coverage, which enhances the potential use of the data. In this study, chemical species were successfully mapped from January to March using O_3, HNO_3, and N_2O data observed with ILAS. HNO_3 is especially important in determining the exact amounts of ozone loss because ozone loss is affected by HNO_3 concentration through ClO_x deactivation and PSC formation. However, the microphysics of PSCs as well as HNO_3-related chemistry are not well understood and are still under investigation [*Gao et al.*, 1999; *Salcedo et al.*, 2001], making the modeling of HNO_3 concentration difficult. We used colocated measurements of HNO_3 to initialize the model, and obtained a more realistic estimate of ozone loss. Details of the chemical box model are given in section 2, and the CSMT technique is explained and validated in section 3. Results are discussed in section 4 and concluding remarks are in section 5.

2. Photochemical Box Model

[9] In a numerical simulation of atmospheric chemical transport, an integration of a set of ordinary differential equations describing chemical transformations is needed. Several techniques to integrate such systems efficiently have been developed. For example, RODAS (Runge-Kutta-Rosenbrock Solver) [*Sandu et al.*, 1997a, 1997b] is well suited for application to atmospheric simulations and offers good accuracy and efficiency and is used in this study. The solver was provided by the Atmospheric Chemistry Division of the National Center of Atmospheric Research (ACD/NCAR). RODAS uses a Runge-Kutta method to calculate implicitly the temporal evolution of chemical minor species. We incorporated 59 chemical species (Appendix A), 101 gas-phase reactions (Table 1), 48 photodissociations (Table 2), and 7 heterogeneous reactions (Table 3) into the model. The code to calculate the photodissociation coefficients (J) is based on the Garcia-Solomon two-dimensional model [*Solomon et al.*, 1985]. Kinetic rates for gas-phase reactions and absorption cross-sections for photodissociation coefficients are from *DeMore et al.* [1997] and *Sander et al.*

Table 1. Gas-Phase Chemical Reactions Included in the Model With the Corresponding Reaction Rates and References[a]

	Reaction	Rate Coefficient	Reference
(1)	$O + O + M \rightarrow O_2 + M$	4.23e-28 × (1./T) × (1./T) × A	JPL94
(2)	$O + O_2 + M \rightarrow O_3 + M$	(6.e-34,2.4,1.,0.) × 0.2095	JPL00
(3)	$O + O_3 \rightarrow 2O_2$	8.e-12 × exp(−2060./T)	JPL97
(4)	$O(^1D) + M \rightarrow O + M$	0.2095 × 3.2e-11 × exp(70./T) + 0.7905 × 1.8e-11 × exp(110./T)	JPL97
(5)	$CH_4 + OH \rightarrow CH_3 + H_2O$	2.45e-12 × exp(−1775./T)	JPL97
(6)	$CH_3 + O_2 + M \rightarrow CH_3O_2 + M$	(4.5e-31,3.,1.8e-12,1.7) × 0.2095	JPL97
(7)	$CH_3O_2 + NO \rightarrow CH_3O + NO_2$	3.0e-12 × exp(280./T)	JPL97
(8)	$CH_3O_2 + CH_3O_2 \rightarrow 2CH_3O + O_2$	2.5e-13 × exp(190./T) × 0.3	JPL97
(9)	$CH_3O_2 + CH_3O_2 \rightarrow CH_2O + CH_3OH + O_2$	2.5e-13 × exp(190./T) × 0.6	JPL97
(10)	$CH_3O + O_2 \rightarrow CH_2O + HO_2$	3.9e-14 × exp(−900/T) × 0.2095	JPL97
(11)	$CH_3O + NO_2 + M \rightarrow CH_3ONO_2 + M$	(1.1e-28,4.,1.6e-11,1.)	JPL97
(12)	$CH_3O_2 + HO_2 \rightarrow CH_3OOH + O_2$	3.8e-13 × exp(800./T)	JPL97
(13)	$CH_3OOH + OH \rightarrow CH_3O_2 + H_2O$	3.8e-12 × exp(200./T) × 0.7	JPL97
(14)	$CH_2O + OH \rightarrow CHO + H_2O$	1.0e-11	JPL97
(15)	$CH2O + O \rightarrow CHO + OH$	3.4e-11 × exp(−1600./T)	JPL97
(16)	$CH2O + Cl \rightarrow HCl + CHO$	8.1e-11 × exp(−30./T)	JPL97
(17)	$CH_2O + NO_3 \rightarrow CHO + HNO_3$	5.8e-16	JPL97
(18)	$CHO + O_2 \rightarrow CO + HO_2$	3.5e-12 × exp(140/T) × 0.2095	JPL97
(19)	$CO + OH \rightarrow HO_2 + CO_2$	1.5e-13 × (1. + 0.6 × (press./1013.))	JPL97
(20)	$CH_4 + O(^1D) \rightarrow CH_3 + OH$	1.5e-10 × 0.75	JPL97
(21)	$CH_4 + O(^1D) \rightarrow CH_2O + H_2$	1.5e-10 × 0.05	JPL97
(22)	$CH_4 + O(^1D) \rightarrow CH_3O + H$	1.5e-10 × 0.2	JPL97
(23)	$H_2O + O(^1D) \rightarrow 2OH$	2.2e-10	JPL00
(24)	$H_2 + O(^1D) \rightarrow H + OH$	1.1e-10	JPL97
(25)	$H + O_2 + M \rightarrow HO_2 + M$	(5.7e-32,1.6,7.5e-11,0.) × 0.2095	JPL97
(26)	$OH + HO_2 \rightarrow H_2O + O_2$	4.8e-11 × exp(250./T)	JPL00
(27)	$OH + HNO_3 \rightarrow H_2O + NO_3$	(X1 + X3/(1. + X3/X2)) X1 = 2.4e-14 × exp(460./T) X2 = 2.7e-17 × exp(2199./T) X3 = 6.5e-34 × exp(1335./T) × A	JPL00
(28)	$OH + NO_2 + M \rightarrow HNO_3 + M$	(2.4e-30,3.1,1.7e-11,2.1)	JPL00
(29)	$HO_2 + NO_2 + M \rightarrow HO_2NO_2 + M$	(1.8e-31,3.2,4.7e-12,1.4)	JPL97
(30)	$HO_2NO_2 + M \rightarrow HO_2 + NO_2 + M$	(29)/(2.1e-27 × exp(10900./T) × A)	JPL97
(31)	$HCl + OH \rightarrow H_2O + Cl$	2.6e-12 × exp(−350./T)	JPL97
(32)	$ClO + HO_2 \rightarrow HOCl + O_2$	4.8e-13 × exp(700./T)	JPL97
(33)	$H + O_3 \rightarrow OH + O_2$	1.4e-10 × exp(−470./T)	JPL97
(34)	$OH + O \rightarrow O_2 + H$	2.2e-11 × exp(120./T)	JPL97
(35)	$HO_2 + O \rightarrow O_2 + OH$	3.e-11 × exp(200./T)	JPL00
(36)	$OH + O_3 \rightarrow HO_2 + O_2$	1.5e-12 × exp(−880./T)	JPL00
(37)	$HO_2 + O_3 \rightarrow OH + 2O_2$	2.e-14 × exp(−680./T)	JPL00
(38)	$HO_2 + NO \rightarrow OH + NO_2$	3.5e-12 × exp(250./T)	JPL97
(39)	$HO_2 + HO_2 \rightarrow H_2O_2 + O_2$	2.3e-13 × exp(600./T) + 1.7e-33 × exp(1000./T) × A	JPL97
(40)	$H_2O_2 + OH \rightarrow HO_2 + H_2O$	2.9e-12 × exp(−160./T)	JPL97
(41)	$OH + N \rightarrow NO + H$	5.e-11	JPL97
(42)	$OH + H_2 \rightarrow H_2O + H$	5.5e-12 × exp(−2000./T)	JPL97
(43)	$N_2O + O(^1D) \rightarrow 2 \times NO$	6.7e-11	JPL00
(44)	$N_2O + O(^1D) \rightarrow N_2 + O_2$	4.9e-11	JPL00
(45)	$N + O_2 \rightarrow NO + O$	1.5e-11 × exp(−3600./T)	JPL97
(46)	$N + NO \rightarrow N_2 + O$	2.1e-11 × exp(100./T)	JPL97
(47)	$NO + O_3 \rightarrow NO_2 + O_2$	3.0e-12 × exp(−1500./T)	JPL00
(48)	$NO_2 + O \rightarrow NO + O_2$	5.6e-12 × exp(180./T)	JPL00
(49)	$NO_2 + O_3 \rightarrow NO_3 + O_2$	1.2e-13 × exp(−2450./T)	JPL97
(50)	$NO_2 + NO_3 + M \rightarrow N_2O_5 + M$	(2.e-30,4.4,1.4e-12,0.7)	JPL00
(51)	$N_2O_5 + M \rightarrow NO_2 + NO_3 + M$	(50)/(3.e-27 × exp(10991/T) × A)	JPL00
(52)	$CH_3Cl + OH \rightarrow H_2O + Cl$	4.0e-12 × exp(−1400./T)	JPL97
(53)	$CH_3CCl_3 + OH \rightarrow H_2O + 3 \times Cl$	1.8e-12 × exp(−1550./T)	JPL97
(54)	$CCl_4 + O(^1D) \rightarrow ClO$	3.3e-10 × 0.9	JPL97
(55)	$CCl_4 + O(^1D) \rightarrow O + CCl_4$	3.3e-10 × 0.1	JPL97
(56)	$CFC11 + O(^1D) \rightarrow ClO$	2.3e-10 × 0.9	JPL97
(57)	$CFC11 + O(^1D) \rightarrow O + CFC11$	2.3e-10 × 0.1	JPL97
(58)	$CFC12 + O(^1D) \rightarrow ClO$	1.4e-10 × 0.9	JPL97
(59)	$CFC12 + O(^1D) \rightarrow O + CFC12$	1.4e-10 × 0.1	JPL97
(60)	$CFC113 + O(^1D) \rightarrow ClO$	2.e-10 × 0.9	JPL97
(61)	$HCFC22 + O(^1D) \rightarrow ClO$	1.0e-10 × 0.9	JPL97
(62)	$HCFC22 + O(^1D) \rightarrow O + HCFC22$	1.0e-10 × 0.1	JPL97
(63)	$HCFC22 + OH \rightarrow H_2O$	1.2e-12 × exp(−1650./T)	JPL97
(64)	$HCFC141 + O(^1D) \rightarrow ClO$	2.6e-10 × 0.9	JPL97
(65)	$HCFC141 + O(^1D) \rightarrow O + HCFC141$	2.6e-10 × 0.1	JPL97
(66)	$HCFC142B + OH \rightarrow H_2O$	1.3e-12 × exp(−1800./T)	JPL97
(67)	$HCFC142B + O(^1D) \rightarrow ClO$	2.2e-10 × 0.9	JPL97
(68)	$HCFC142B + O(^1D) \rightarrow HCFC142B + O$	2.2e-10 × 0.1	JPL97
(69)	$CH_4 + Cl \rightarrow HCl + CH_3$	9.6e-12 × exp(−1360./T)	JPL00
(70)	$Cl + O_3 \rightarrow ClO + O_2$	2.3e-11 × exp(−200./T)	JPL00

Table 1. (continued)

	Reaction	Rate Coefficient	Reference
(71)	$ClO + O \rightarrow Cl + O_2$	3.0e-11 × exp(70./T)	JPL00
(72)	$ClO + NO \rightarrow Cl + NO_2$	6.4e-12 × exp(290./T)	JPL97
(73)	$Cl + H_2 \rightarrow HCl + H$	3.7e-11 × exp(−2300./T)	JPL97
(74)	$Cl + HO_2 \rightarrow HCl + O_2$	1.8e-11 × exp(170./T)	JPL97
(75)	$Cl + H_2O_2 \rightarrow HCl + HO_2$	1.1e-11 × exp(−980./T)	JPL97
(76)	$HCl + O \rightarrow OH + Cl$	1.0e-11 × exp(−3300./T)	JPL97
(77)	$ClO + NO_2 + M \rightarrow ClONO_2 + M$	(1.8e-31,3.4,1.5e-11,1.9)	JPL97
(78)	$HOCl + OH \rightarrow H_2O + ClO$	3.0e-12 × exp(−500./T)	JPL97
(79)	$ClO + ClO + M \rightarrow Cl_2O_2 + M$	(1.59e-32,4.5,1.36e-12,3.09)	*Bloss et al.* [2001]
(80)	$ClOO + M \rightarrow Cl + O_2 + M$	(2.7e-33,1.5,1,0)/(5.7e-25 × exp(2500./T) × A)	JPL97
(81)	$Cl_2O_2 + M \rightarrow 2 \times ClO + M$	(79)/(1.27e-27 × exp(8744./T) × A)	JPL00
(82)	$ClO + OH \rightarrow HO_2 + Cl$	7.4e-12 × exp(270./T)	JPL00
(83)	$ClO + OH \rightarrow HCl + O_2$	3.2e-13 × exp(320./T)	JPL00
(84)	$ClO + ClO \rightarrow OClO + Cl$	3.5e-13 × exp(−1370./T)	JPL97
(85)	$ClO + ClO \rightarrow ClOO + Cl$	3.0e-11 × exp(−2450./T)	JPL97
(86)	$ClO + ClO \rightarrow Cl_2 + O_2$	1.0e-12 × exp(−1590./T)	JPL97
(87)	$Br + O_3 \rightarrow BrO + O_2$	1.7e-11 × exp(−800./T)	JPL97
(88)	$BrO + O \rightarrow Br + O_2$	1.9e-11 × exp(230./T)	JPL97
(89)	$BrO + NO \rightarrow Br + NO_2$	8.8e-12 × exp(260./T)	JPL97
(90)	$BrO + ClO \rightarrow Br + OClO$	9.5e-13 × exp(550./T)	JPL00
(91)	$BrO + ClO \rightarrow Br + ClOO$	2.3e-12 × exp(260./T)	JPL00
(92)	$BrO + ClO \rightarrow BrCl + O_2$	4.1e-13 × exp(290./T)	JPL00
(93)	$BrO + BrO \rightarrow 2 \times Br + O_2$	2.4e-12 × exp(40./T)	JPL97
(94)	$Br + HO_2 \rightarrow HBr + O_2$	1.5e-11 × exp(−600./T)	JPL97
(95)	$Br + H_2O_2 \rightarrow HBr + HO_2$	1.e-11 × exp(−3000./T)	JPL97
(96)	$HBr + OH \rightarrow Br + H_2O$	1.1e-11	JPL97
(97)	$HBr + O \rightarrow Br + OH$	5.8e-12 × exp(−1500./T)	JPL97
(98)	$BrO + NO_2 + M \rightarrow BrONO_2 + M$	(5.2e-31,3.2,6.9e-12,2.9)	JPL97
(99)	$BrO + HO_2 \rightarrow HOBr + O_2$	3.4e-12 × exp(540./T)	JPL97
(100)	$Br + CH_2O \rightarrow HBr + CHO$	1.7e-11 × exp(−800./T)	JPL97
(101)	$CH_3Br + OH \rightarrow Br$	4.e-12 × exp(−1470./T)	JPL97

[a]A, air number density; press, pressure (hPa). JPL94 represents *DeMore et al.* [1994], JPL97 represents *DeMore et al.* [1997], and JPL00 represents *Sander et al.* [2000]. Reactions of CFC and HCFC with $O(^1D)$ were assumed to produce ClO with a quantum yield of 0.9, and the other branch was assumed to be quenched [*Warren et al.*, 1991]. Three body reaction rates are expressed for (a, b, c, and d) as: $k = x_1 \cdot 0.6^{x_2}$; $k_0(t) = a \cdot (\frac{t}{300})^{-b}$; $k_\infty(t) = c \cdot (\frac{t}{300})^{-d}$; $x_1 = \frac{k_0(t)\cdot A}{1+(k_0(t)\cdot A/k_\infty(t))}$; and $x_2 = (1 + (\log_{10}(\frac{k_0(t)\cdot A}{k_\infty(t)}))^2)^{-1}$.

[2000] except a reaction rate of ClO + ClO + M (reaction 79 in Table 1) which was recently updated by *Bloss et al.* [2001] (Appendix A; Table 1).

[10] Polar chemistry is very sensitive to sunlight. Thus ultraviolet radiation for large solar zenith angles (SZA) was carefully examined before the model was applied to polar regions in winter and spring. The air mass factor when the SZA exceeded 90° was determined using the Chapman function (see Appendix B).

[11] PSC growth governed by the temperature change along trajectories is included in the calculations. Supercooled ternary solutions (STS) are assumed because STS are the most likely event in the Arctic stratosphere [e.g., *Dye et al.*, 1992]. Nitric acid trihydrate (NAT) is assumed to be present because NAT is also observed [e.g., *Fahey et al.*, 2001]. PSCs are included based on thermodynamic equilibrium [*Carslaw et al.*, 1995; *Hanson and Mauersberger*, 1988]. However, PSC formation mechanisms are poorly understood. As discussed in many studies [e.g., *Tolbert*, 1994, 1996], NAT does not form at thermodynamic equilibrium, and there is no definite scheme to model NAT formation. In this study, a control run included STS formation according to the thermodynamic theory of *Carslaw et al.* [1995]; other runs were performed to examine the effects of NAT and a possible warm bias in the temperature data set. *Saitoh et al.* [2002] found many STS events in mid-January at altitudes of 20–23 km and some evidence of NAT/nitric acid dehydrate (NAD) in early March at altitudes of 16–18 km in the ILAS aerosol data. We will discuss the PSC effect on ozone destruction by comparison with those results. A surface-to-mass conversion factor that is based on size distribution functions measured with an optical particle counter (OPC) that same winter [*Deshler et al.*, 2000] was derived to help estimate heterogeneous reaction rates. Mean radii and standard deviations for STS, NAT, and background sulfate aerosol in lognormal size distribution functions are shown in Table 4. The reaction probabilities (γ) for the seven heterogeneous reactions listed in Table 3 were determined for liquid droplets [*Hanson*, 1998] and NAT [*DeMore et al.*, 1997]. The reaction probabilities for STS were taken from the data for sulfuric acid droplets because the data for STS were not available (Tables 3 and 4).

3. Chemical Species Mapping on Trajectories (CSMT)

3.1. CSMT Scheme

[12] CSMT constructs synoptic maps of chemical species by combining "trajectory mapping" [*Morris et al.*, 1995, 2000] with a photochemical box model. Minor constituents are time-integrated in a photochemical box model along trajectories that evolve from satellite measurement points until a target time. Combining a chemical model with trajectory mapping allows the creation of synoptic maps of all long-lived species, and of some short-lived species as well, such as ClO.

[13] Trajectories in this study were calculated by the Earth Observation Research Center Trajectory Analysis

Table 2. Photodissociation Reactions Included in the Model[a]

Number	Photolysis
(1)	$O_2 + h\nu \rightarrow 2O$
(2)	$O_3 + h\nu \rightarrow O_2 + O(^1D)$
(3)	$O_3 + h\nu \rightarrow O_2 + O$
(4)	$CH_4 + h\nu \rightarrow CH_3 + H$
(5)	$CH_4 + h\nu \rightarrow CH_2 + H_2$
(6)	$CH_4 + h\nu \rightarrow CH + H_2 + H$
(7)	$CH_3OOH + h\nu \rightarrow CH_3O + OH$
(8)	$CH_2O + h\nu \rightarrow H + CHO$
(9)	$CH_2O + h\nu \rightarrow H_2 + CO$
(10)	$CO_2 + h\nu \rightarrow CO + O$
(11)	$H_2O + h\nu \rightarrow H + OH$
(12)	$H_2O_2 + h\nu \rightarrow 2OH$
(13)	$HO_2NO_2 + h\nu \rightarrow OH + NO_3$
(14)	$N_2O + h\nu \rightarrow N_2 + O(^1D)$
(15)	$NO + h\nu \rightarrow N + O$
(16)	$NO_2 + h\nu \rightarrow NO + O$
(17)	$NO_3 + h\nu \rightarrow NO + O_2$
(18)	$NO_3 + h\nu \rightarrow NO_2 + O$
(19)	$N_2O_5 + h\nu \rightarrow NO + O + NO_3$
(20)	$N_2O_5 + h\nu \rightarrow NO_2 + NO_3$
(21)	$HNO_3 + h\nu \rightarrow OH + NO_2$
(22)	$HO_2NO_2 + h\nu \rightarrow HO_2 + NO_2$
(23)	$CH_3Cl + h\nu \rightarrow Cl + CH_3$
(24)	$CH_3Br + h\nu \rightarrow Br + CH_3$
(25)	$CCl_4 + h\nu \rightarrow 4Cl$
(26)	$CH_3CCl_3 + h\nu \rightarrow 3Cl$
(27)	$CFC11 + h\nu \rightarrow 3Cl$
(28)	$CFC12 + h\nu \rightarrow 2Cl$
(29)	$CFC113 + h\nu \rightarrow 3Cl$
(30)	$CFC114 + h\nu \rightarrow 3Cl$
(31)	$CFC115 + h\nu \rightarrow 3Cl$
(32)	$HCFC22 + h\nu \rightarrow Cl$
(33)	$HCFC142B + h\nu \rightarrow Cl$
(34)	$HAL1211 + h\nu \rightarrow Br + Cl$
(35)	$HAL1301 + h\nu \rightarrow Br$
(36)	$HCl + h\nu \rightarrow H + Cl$
(37)	$ClONO_2 + h\nu \rightarrow Cl + NO_3$
(38)	$HOCl + h\nu \rightarrow OH + Cl$
(39)	$Cl_2O_2 + h\nu \rightarrow Cl + ClOO$
(40)	$Cl_2 + h\nu \rightarrow 2Cl$
(41)	$ClONO_2 + h\nu \rightarrow ClO + NO_2$
(42)	$OClO + h\nu \rightarrow ClO + O$
(43)	$BrCl + h\nu \rightarrow Br + Cl$
(44)	$BrO + h\nu \rightarrow Br + O$
(45)	$HBr + h\nu \rightarrow Br + H$
(46)	$HOBr + h\nu \rightarrow Br + O_2H$
(47)	$BrONO_2 + h\nu \rightarrow BrO + NO_2$
(48)	$BrONO_2 + h\nu \rightarrow Br + NO_3$

[a]Quantum yield of $O(^1D)$ by ozone photodissociation (2) is parameterized from *Sander et al.* [2000].

Table 4. Mean Radii and Standard Deviations of Aerosol Size Distributions Used to Calculate Surface Areas From the Volumes of STS, NAT, and Sulfate (Background) Aerosol

	Mean Radius, μm	Standard Deviation
STS[a]	0.29	1.45
NAT[a]	1.73	1.33
Sulfuric acid[b]	0.08	1.80

[a]From *Deshler et al.* [2000].
[b]From *Hofmann and Rosen* [1984].

Model (EORC-TAM) [*Matsuzono et al.*, 1998] with meteorological data sets from the European Center for Medium-Range Weather Forecasts (ECMWF/TOGA basic level III data). These data sets include twice a day (0 and 12 UTC) at a horizontal resolution of 2.5° latitude and longitude. *Morris et al.* [1995] discussed trajectory dispersion and noted that most trajectories were compact before ~10 days, even in the Northern Hemisphere winter. Figure 1 is comparable to *Morris et al.* [1995, Figure 1], showing the ratio of air parcels (20 km × 20 km) that keep megaparcels "compact" for the duration of the trajectory when all trajectories are calculated. Each megaparcel includes one central trajectory which starts at an ILAS measurement location surrounded by four additional trajectories. The starting points of the four additional trajectories are 20 km from ILAS measurement location in the north, south, east, and west directions. A megaparcel is defined as compact if all four trajectories remain within 400 km of the central trajectory. Figure 1 indicates that trajectories for less than about ten days sustain enough reliability inside the polar vortex as discussed by *Morris et al.* [1995]. In this study we used seven-day trajectories to create maps for chemical species, to maintain reliability in trajectory calculations even during the period of polar vortex development in January (Figure 1).

[14] Diabatic descent is ignored in the present scheme for seven-day trajectories. Rates of descent estimated from ILAS N_2O data [*Kanzawa et al.*, 2000] and from other data sources [e.g., *Knudsen et al.*, 1998] are sufficiently small (~147 m based on the value from *Kanzawa et al.* [2000] and ~400 m from *Knudsen et al.* [1998]) that descent can be neglected in trajectories covering seven days. Indeed, the obtained CSMT-derived data for each day are from trajectories that span less than seven days.

[15] The initial values of ozone, HNO_3, and N_2O at the initial trajectory points are taken from ILAS version 5.20 data. Inversion algorithms used in ILAS version

Table 3. Heterogeneous Reactions and the Reaction Probabilities Used in the Model

		Reaction Probability	
	Heterogeneous Reaction	Sulfuric Acid	NAT
(1)	$N_2O_5 + H_2O(aer) \rightarrow 2HNO_3$	0.10[a]	0.40×10^{-5}[b]
(2)	$ClONO_2 + HCl \rightarrow Cl_2 + HNO_3$	0.30 (192K)[c]	0.20[b]
(3)	$ClONO_2 + H_2O(aer) \rightarrow HOCl + HNO_3$	0.57×10^{-2} (192K)[c]	0.40×10^{-2}[b]
(4)	$HOCl + HCl \rightarrow Cl_2 + H_2O$ (aer)	0.51 (192K)[c]	0.10[b]
(5)	$BrONO_2 + H_2O(aer) \rightarrow HOBr + HNO_3$	0.80 (192K)[c]	0.60×10^{-2}[d]
(6)	$HOBr + HCl \rightarrow BrCl + H_2O$ (aer)	1.00 (192K)[c]	0.10[d]
(7)	$BrONO_2 + HCl \rightarrow BrCl + HNO_3$	0.90[a]	0.30[d]

[a]From *DeMore et al.* [1997]. γ was calculated assuming P = 50 hPa, H_2O = 5.0 ppmv, and HCl = 2.0 ppbv.
[b]From *Sander et al.* [2000].
[c]From *Hanson* [1998].
[d]From *Lary et al.* [1996].

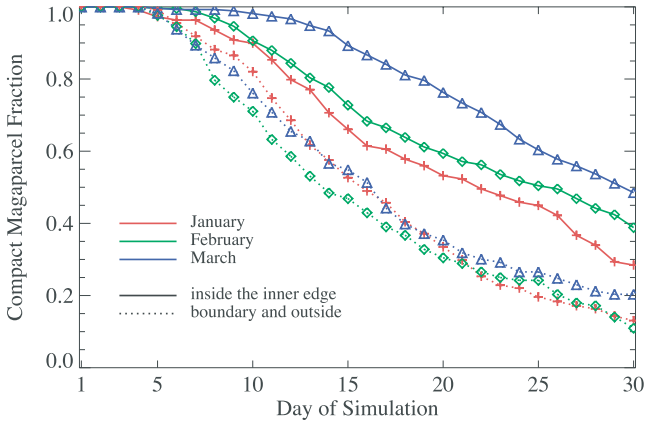

Figure 1. The fraction of air parcels that keep compact megaparcels for the trajectory duration as a function of time on the 475 K isentropic surface. Trajectories were calculated using ECMWF winds during January to March 1997. Red, green, and blue lines indicate the fraction of compact megaparcel trajectories for January, February, and March, respectively. Solid lines show trajectory calculations at the inside of the inner edge of the polar vortex. Dashed lines show at the boundary region and at the outside of the outer edge of the polar vortex.

5.20 data are detailed in the work of *Yokota et al.* [2002], who reported a root-sum-square total uncertainty of 9% for ozone data at 20 km. Ozone data quality in ILAS version 5.20 was validated by *Sugita et al.* [2002], who compared ILAS data with many other measurements, and found agreement to within 10%. Comparisons between balloon-borne measurements of HNO_3 and ILAS HNO_3 data were discussed by *Koike et al.* [2000] for version 3.1, and by *Irie et al.* [2002] for version 5.20. Although ILAS version 5.20 ozone and HNO_3 measurements were confirmed in the latter validation study, ozone can have a large positive bias of 0.9 ppmv at 20 km when ice PSCs are simultaneously observed [*Yokota et al.*, 2002]. However, this ozone bias is unimportant in the present analysis because temperatures did not reach ice-formation temperatures at ILAS measurement latitudes in 1997. Ice PSC formation was noted nowhere in ILAS aerosol measurements [*Saitoh et al.*, 2002] except for a limited area downwind of the Scandinavian mountains in mid-January [*Pan et al.*, 2002; *Saitoh et al.*, 2002].

[16] The amount of column ozone above the target altitude controls the ultraviolet radiation and all photodissociation coefficients at the target altitude, and was estimated from the ILAS ozone profile at the starting trajectory point. Total chlorine and bromine at 475 K were set to 3.0 ppbv, and 20.0 pptv, respectively, values from a recent WMO report [*WMO*, 1999].

[17] Initial values of other species were taken from a statistical analysis of calculations on several "representative trajectories," a method similar to the "idealized trajectory" of *Becker et al.* [1998]. Thirty-six representative trajectories were calculated from 25 December 1996 to 31 May 1997, at 10° longitude intervals with starting points at latitude 75°N. Initial values of the chemical calculations on representative trajectories for CH_4 and H_2O were taken from the averaged values of the Halogen Occultation Experiment (HALOE) data (version 19) observed in the polar vortex from March to April 1997. The initial values of other species were taken from the output of a one-dimensional model that was supplied by Susan Solomon at the NOAA Aeronomy Laboratory. The "representative initial values" for all short-lived species were obtained from calculations for the representative trajectories using output every 6 hours. Outputs of short-lived species were smoothed with a four-day running mean on each trajectory, and the output from the 36 trajectories were averaged for each day north of 60°N. The data set obtained was set as the representative initial value for later calculations.

[18] Additional time integrations adjusted short-lived species to the atmospheric conditions at the starting points. Trajectories for seven days are calculated from each ILAS observation point from January to March. On all trajectories, the photochemical box model calculates the time evolution of the chemical species. All chemical species calculated for a target day were combined to create a synoptic map. Figure 2 shows examples of CSMT-derived maps of Arctic ozone on the 475 K isentropic surface for every 10 days from January through March. Mixing ratios were averaged if more than one data value occupied the same 2.5 × 2.5° grid box. Polar vortex boundaries were determined by a method similar to that of *Nash et al.* [1996] and archived at the ILAS/Data Handling Facility (DHF). The three solid lines in each panel represent the inner edge of the vortex boundary, the peak vortex edge, and the outer edge of the vortex boundary. Blank areas represent no data for mapping. ILAS was an occultation sensor on a polar-orbiting satellite; latitudinal coverage was limited at high latitudes near 65–70°N. Nevertheless, the CSMT map with seven-days trajectory calculations covers most of the polar vortex, with a lack of coverage only near the Pole. In January, ozone mixing ratios show uniformly high values of ~3.2 ppmv in the polar vortex. Ozone decreased gradually after mid-February and reached lower values in March in the polar vortex. The distribution of the ozone mixing ratio is not uniform, with lower values at high latitudes in late March (Figure 2).

[19] As described in section 2, PSCs are formed as the air cools along trajectories in the model. The total amounts of HNO_3 and H_2O in gas-phase and particles needed for calculations on the thermodynamic growth of PSCs were estimated from ILAS HNO_3 and H_2O data. Although ILAS measured HNO_3 and H_2O along with aerosols, data that were colocated with PSCs were not used to determine the threshold temperature of PSCs' formation because where PSCs exist there could be a significant bias in the data [*Yokota et al.*, 2002]. A background average was used instead. HNO_3 and H_2O data inside the polar vortex were averaged for each 10-day period in the region where the colocated temperature exceeded 200 K. The average values were taken as the total background amounts including gas and particles of HNO_3 and H_2O [*Hayashida et al.*, 2000b; *Saitoh et al.*, 2002].

[20] To judge the activation of chlorine species at the starting point, results from PSC analysis of ILAS data are utilized [*Saitoh et al.*, 2002]. When a PSC event was observed at the starting point, enhancement of Cl_2, HOCl, HOBr, and BrCl up to 0.4 ppbv, 0.4 ppbv, 5.0 pptv, and 10.0 pptv, respectively, was assumed, which may result in about 1.2 ppbv of ClO_x and about 15.0 pptv BrO_x under

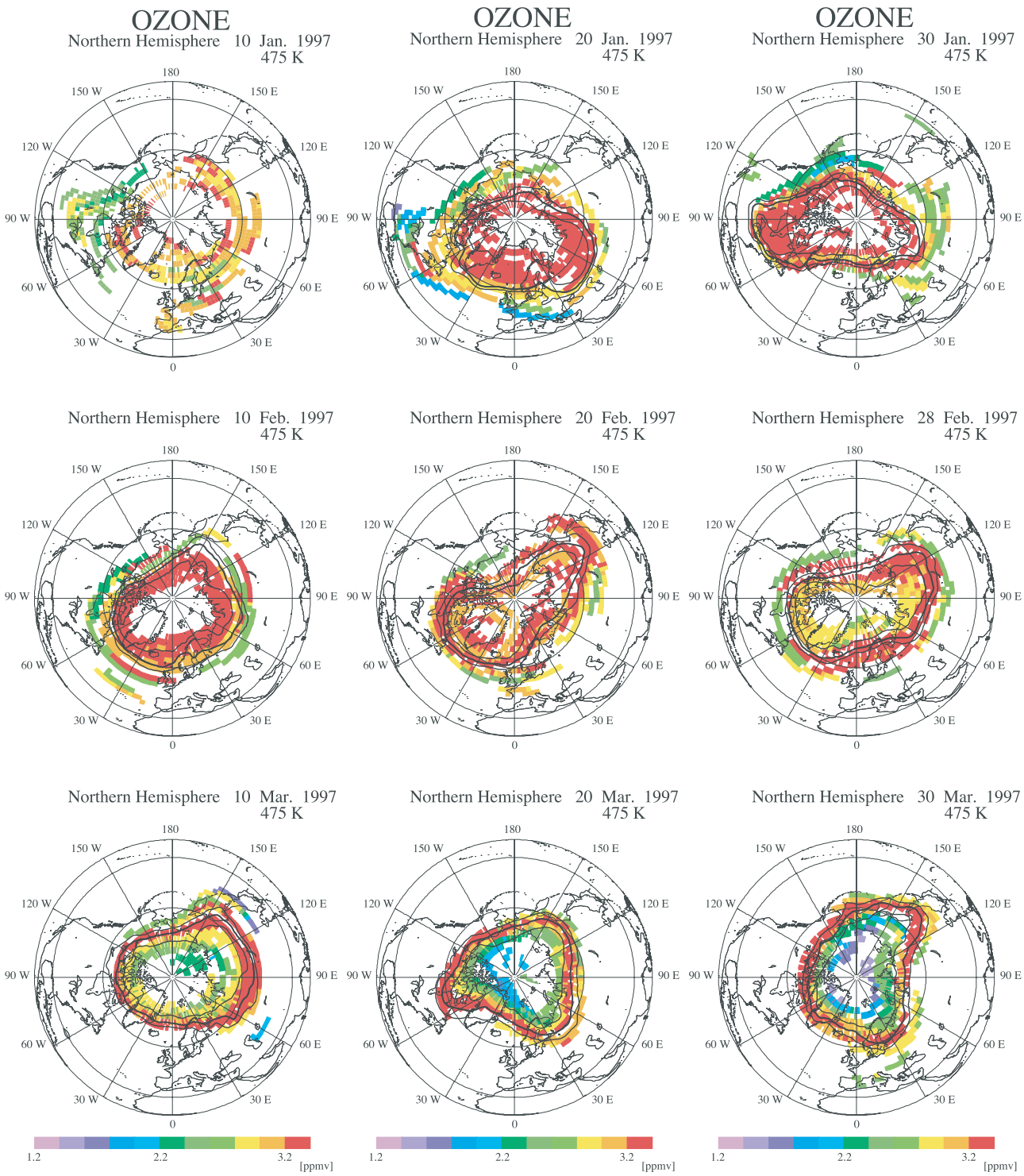

Figure 2. Time series of CSMT maps of ozone obtained every 10 days from January to March in 1997. Colors indicate ozone mixing ratios on the 475 K isentropic surface.

sunlit conditions. However, this assumption may cause underestimation of chlorine activation because PSC might have been formed just before the ILAS measurement time even if ILAS could not observe it. To incorporate the temperature history experienced by air parcels before the trajectory started, backward trajectories were also calculated at all starting points to determine temperature change. When the minimum temperature along the 10-day backward trajectory was less than 195 K, same enhancement of chlorine and bromine are assumed. Though 10-day may be too long to investigate the low temperature experience, there was not essential difference if the period was fixed to three days.

3.2. Comparison of CSMT Ozone With Ozonesonde Data

[21] The ILAS project conducted validation campaigns including ozonesonde soundings at Andoya (69.3°N, 16.1°W), Fairbanks (64.9°N, 147.9°E), Kiruna (67.9°N,

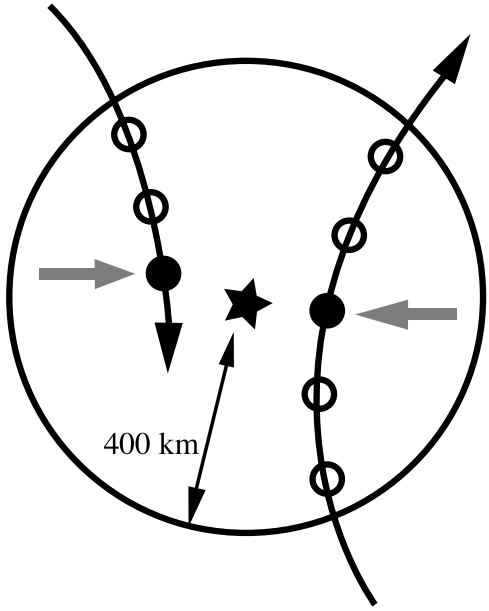

Figure 3. Schematic diagram for selection of the pair of ozone data derived from CSMT and observed with ozonesonde. The CSMT trajectories in a circle of 400 km radius centered on the sonde measurement within ±12 hours were collected. For each trajectory, the CSMT ozone data nearest to the sonde measurement was selected as indicated by gray arrows. The ozone data selected for all such trajectories in the circle are averaged and compared with the ozonesonde data.

21.1°W), and Yakutsk (62.0°N, 129.6°W) for the Northern Hemisphere. These ozonesonde data are archived as ILAS Correlative Measurement Data Base (ILAS-CMDB). *Sugita et al.* [2002] compared ILAS version 5.20 ozone data with them through the "traditional approach" rather than a Lagrangian approach using the Trajectory Hunting Technique as proposed by *Danilin et al.* [2002] because they could find many coincident measurement pairs through the conventional method. They indicated that the ILAS and ozonesonde data agree within 10% between 13 and 30 km, and at the $\theta \sim 475$ K level used in this study, the difference is even less than ~5% [see *Sugita et al.*, 2002, Figure 5a]. The ozonesonde is well-validated and accepted as a precise sensor, so the consistency of ILAS and ozonesonde data underscores the reliability of ILAS version 5.20 ozone data. In the following, we show the comparison of ILAS and ozonesonde measurements thorough a Lagrangian approach as *Danilin et al.* [2002] applied to the comparison of different satellite sensors. This is not to validate ILAS ozone data but to validate the CSMT scheme and its components (the trajectory tool, the meteorological data set, and the chemical box model) used in this study.

[22] We used ozonesonde profiles at Kiruna (51 profiles) and Yakutsk (11 profiles), all of which are archived in the ILAS-CMDB. In the first approach, ILAS and ozonesonde pairs were selected such that time and space differences were limited to ±12 hours and 400 km, respectively. The relative difference in the two-paired data was defined as $D_1 = \frac{\text{Ozone}^{\text{ILAS}} - \text{Ozone}^{\text{sonde}}}{\text{Ozone}^{\text{sonde}}}$ for each pair, and D_1 values for all pairs were averaged ($\bar{D_1}$). Next, we applied trajectory mapping. Ozone mixing ratios are calculated along trajectories from ILAS measurement points at θ = 475 K, 550 K, 700 K, and 750 K. All ozone data (and other species data) at hourly intervals are stored along with trajectory information. For one specific ozonesonde measurement, all isentropic trajectories located within a circle of 400-km radius centered on the sonde measurement location with a time difference of ±12 hours were selected. The nearest point for

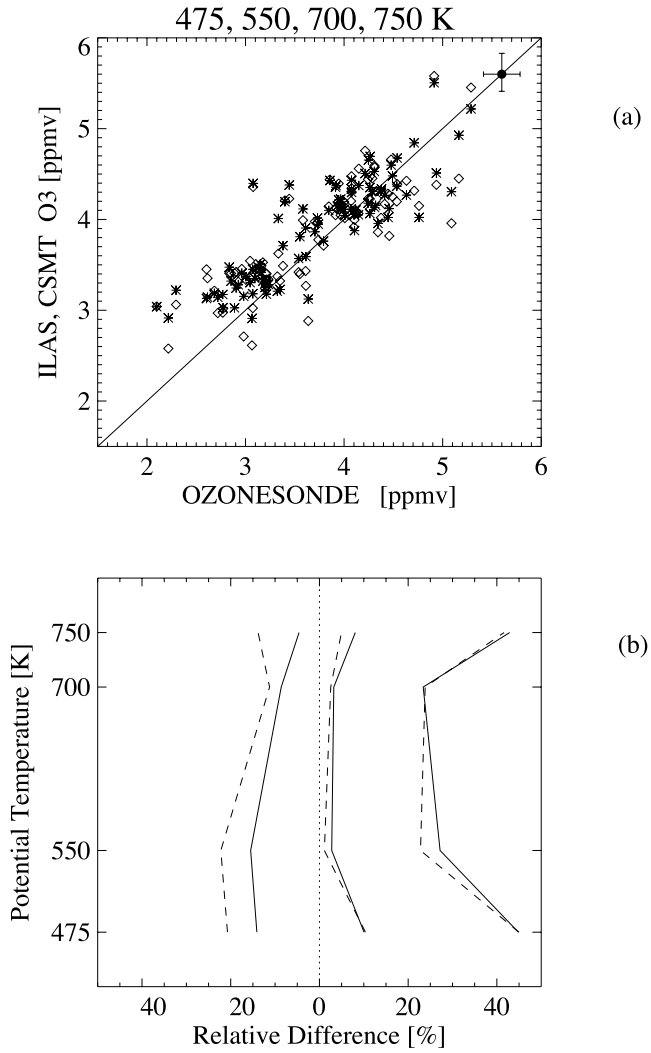

Figure 4. (a) Scatterplot of ozonesonde data versus ILAS or CSMT ozone data at 475, 550, 700, and 750 K. Diamond indicates ILAS versus ozonesonde data selected by the traditional approach. Asterisk shows CSMT ozone versus ozonesonde data selected by the Lagrangian approach. The solid line is the one-to-one line. The averaged error bars of ozonesonde and ILAS data are shown on the one-to-one line with a solid circle. The errors for ILAS and ozonesonde data are the averaged value of each error of the ILAS and sonde data, respectively. Error of ozonesonde data is taken 5% of the value. (b) Relative difference between ozonesonde and ILAS or CSMT ozone at 475, 550, 700, and 750 K. The solid line indicates relative difference between CSMT and ozonesonde data, that is $\bar{D_2}$. The dashed line indicates relative difference between ILAS and ozonesonde data, that is $\bar{D_1}$. The maximum and minimum values of D_1 and D_2 are also shown.

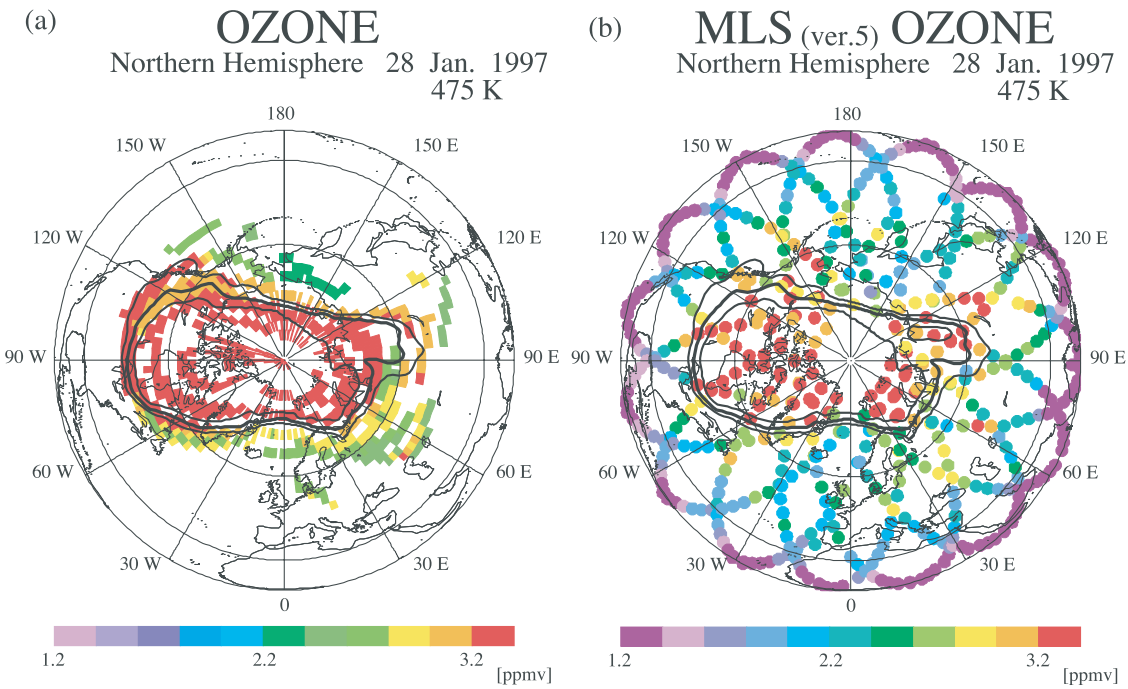

Figure 5. (a) Map of 475 K CSMT ozone (ppmv) on 28 January 1997. In this projection, 0 longitude is at the bottom and the black circles are for 30°N and 60°N. All points are the ozone-mixing ratio (color code is shown in the bar under the map) calculated for 28 January 1997 using about 90 trajectories starting from ILAS measurement points from 21 to 28 January. The blank area represents no data. The three solid lines are the inner boundary, the peak edge, and the outer boundary of the polar vortex provided by ILAS/DHF. (b) The 475 K MLS version 5 ozone (ppmv) on 28 January 1997.

one trajectory was taken as comparable data for the target ozonesonde data. Figure 3 conceptually shows this method. For most cases, about 6 ~ 7 trajectories can be taken for one target sonde measurement, and the nearest point to the target sonde data was taken for each trajectory. The averaged value for those data was defined as the counterpart of the ozonesonde data, and compared in the same way as in the conventional comparison. We can determine $D_2 = \frac{\overline{Ozone^{CSMT}} - Ozone^{sonde}}{Ozone^{sonde}}$ and $\bar{D}_2$ in the same way with D_1 and $\bar{D}_1$ (Figure 3).

[23] Figure 4a presents the scatterplot of ozonesonde data versus ILAS or CSMT ozone data. Diamonds indicate original ILAS data selected using the traditional approach, and asterisks indicate the Lagrangian approach. CSMT data show better correlation to sonde data than ILAS data, which reflects the reliability of trajectory calculations. Unlike Trajectory Mapping (TM), CSMT can provide ozone data at photochemically active altitudes such as 750 K. Figure 4b depicts the relative difference (%) between ozonesonde data and ILAS or CSMT, that is, $\bar{D}_1$ and $\bar{D}_2$. The $\bar{D}_2$ values are comparable to $\bar{D}_1$, and minimum value of D_2 is much larger, which suggests the mapping preserves the reliability of the original ILAS data even after seven days' integration along the trajectories. This suggests the ozone map shown in Figure 2 is reliable, and highlights the accuracy of the CSMT scheme used in this study (Figure 4).

3.3. Comparison of CSMT Maps With MLS Data

3.3.1. Ozone

[24] Figure 5a shows a representative CSMT ozone map for 28 January, before a period of significant chemical ozone destruction in late February and March. *Manney et al.* [1997, Figure 1] shows the Microwave Limb Sounder (MLS) version 4 ozone data at 475 K for the same day. Though the CSMT ozone data have slightly higher values than MLS version 4 data in the work of *Manney et al.* [1997], the recent algorithm of MLS (Version 5) have removed the bias that was in version 4, increasing globally averaged ozone values by about 0.6 ppmv at 46 hPa (MLS version 5 readme file). Figure 5b depicts version 5 MLS data observed on the same day as Figure 5a. Figures 6a and 6b also show the CSMT and MLS version 5 ozone maps observed on 26 February during the significant ozone loss period. There are consistent features in ozone distributions in the CSMT and MLS ozone maps for both 28 January and 26 February as indicated in those figures (Figures 5 and 6).

[25] To compare CSMT ozone values with MLS version 5 data more quantitatively, we applied an approach similar to that used for the ozonesonde comparisons. Original ILAS data and CSMT-derived ozone data within ±12 hours and 400-km were compared to MLS data. Figure 7a is a scatterplot of original MLS versus ILAS data in late January 1997. Red, green, and blue triangles indicate the inside, boundary, and outside of the vortex, respectively. Most of the data selected are consistent within the error bars, though some data are not. More data pairs in the CSMT scheme can be compared with MLS data. Figure 7b superimposes CSMT ozone on Figure 7a. The colored dots in Figure 7b are the scatterplots of MLS ozone and the CSMT-derived ozone that correspond to each MLS data point by averaging 6 ~ 7 data points as in the comparison with ozonesonde data. Some of the ILAS data do not correlate with the

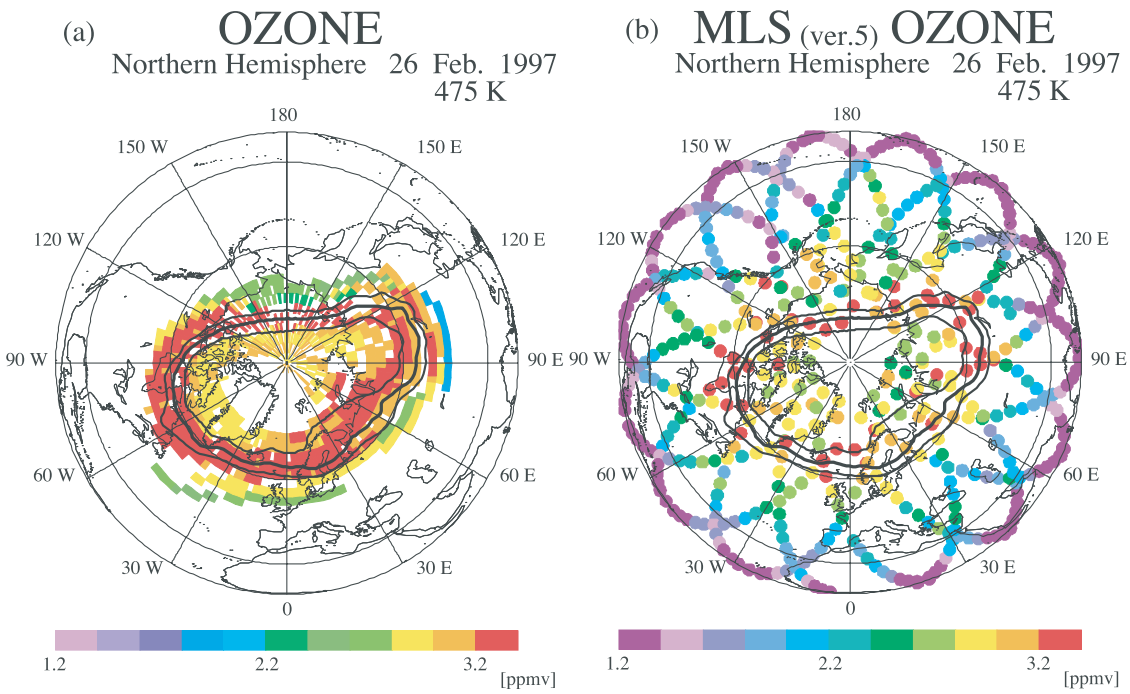

Figure 6. (a) As in Figure 5a but for 26 February. (b) As in Figure 5b but for 26 February.

corresponding MLS data. CSMT-derived ozone initialized by those ILAS data inevitably diverges from the MLS data, as represented by the scattering of colored points around those data, but that is a limit of this scheme. However, most of the CSMT data are within the error range, showing the correlation between CSMT and MLS data. This is further proof of the robustness of the CSMT scheme. Figures 7c and 7d are similar scatterplots for late February. As shown in the figure, most of the points are again in the range of error bars. Though some data points are scattering at far outside of the error range, they are all for outside of the polar vortex, therefore, there is not a significant effect on later analysis of chemical processes inside the vortex. Table 5 summarizes some statistical values for the relation of MLS and CSMT data for all data points shown in Figures 7b and 7d. The correlation coefficient for late February is not efficient enough but this is due to the limited data range, and the root-mean square (RMS) difference indicates enough reliability of the CSMT data. Table 5 also demonstrates the CSMT scheme does not derive any systematic bias (Table 5 and Figure 7).

3.3.2. Nitric Acid

[26] Figure 8a shows CSMT HNO_3 for 28 January. The comparable MLS (version 4) data at 465 K on the same day are presented in the work of *Santee et al.* [1997]. *Santee et al.* [1997, Figures 8a and 2] depict HNO_3 mixing ratios as high as ~12 ppbv almost everywhere within the polar vortex. Figures 8b depicts version 5 MLS data at 475 K on the same day as Figure 8a, which again indicates the good correlation of the two maps. Figure 9a shows CSMT HNO_3 for 20 February. This is comparable to the MLS HNO_3 (version 4) for the same day as in the work of *Santee et al.* [1997, Figure 2]. Figure 9b depicts version 5 MLS data at 475 K on the same day as in Figure 8b. The notable decrease in CSMT HNO_3 to ~2 ppbv (shown in violet) deep inside the vortex, which is associated with low temperatures and uptake into PSCs in the model, agrees with the low nitric acid values in the MLS map for the same day (Figures 8 and 9).

[27] We now compare the CSMT HNO_3 values with MLS version 5 data more quantitatively. Figure 10 is similar to Figure 7 but for nitric acid. Figures 10a and 10c depict scatterplots of the original MLS and ILAS data in late January and late February, respectively. Figures 10b and 10d superimpose CSMT HNO_3 on Figures 10a and 10c, which highlight the good correlation of CSMT-derived nitric acid data with MLS version 5 data. Though the precision of MLS version 5 data at 46 hPa is 1 ppbv (MLS version 5 readme file), the one-to-one correlation line should be shifted to the right in the figure because *Danilin et al.* [2002] reported that the MLS version 5 data were larger than the original ILAS version 5.20 data by ~1 ppbv near 475 K. Most of the scattered data are within the range of the error bars, although some of the original ILAS data lie outside the range. CSMT-derived data initialized by those ILAS data are inevitably outside the range of the error as discussed on ozone. Nevertheless, the good correlation observed in Figure 10b demonstrates how well CSMT nitric acid data match MLS data. For late February, the nitric acid data inside the vortex scatter in wide range. Some nitric acid data indicate very low values as in Figure 10d because significant denitrification occurred during the period [*Kondo et al.*, 2000]. As described in the previous section, we can reproduce those denitrified situations even without a sophisticated model of PSC growth and sedimentation because denitrification is involved implicitly in our analysis by initializing chemical model with the really observed nitric acid. This result again demonstrates the advantage of CSMT (Figure 10).

3.3.3. Chlorine Monoxide

[28] Minor constituents, including radicals, can be derived in the same way, but not all are presented here.

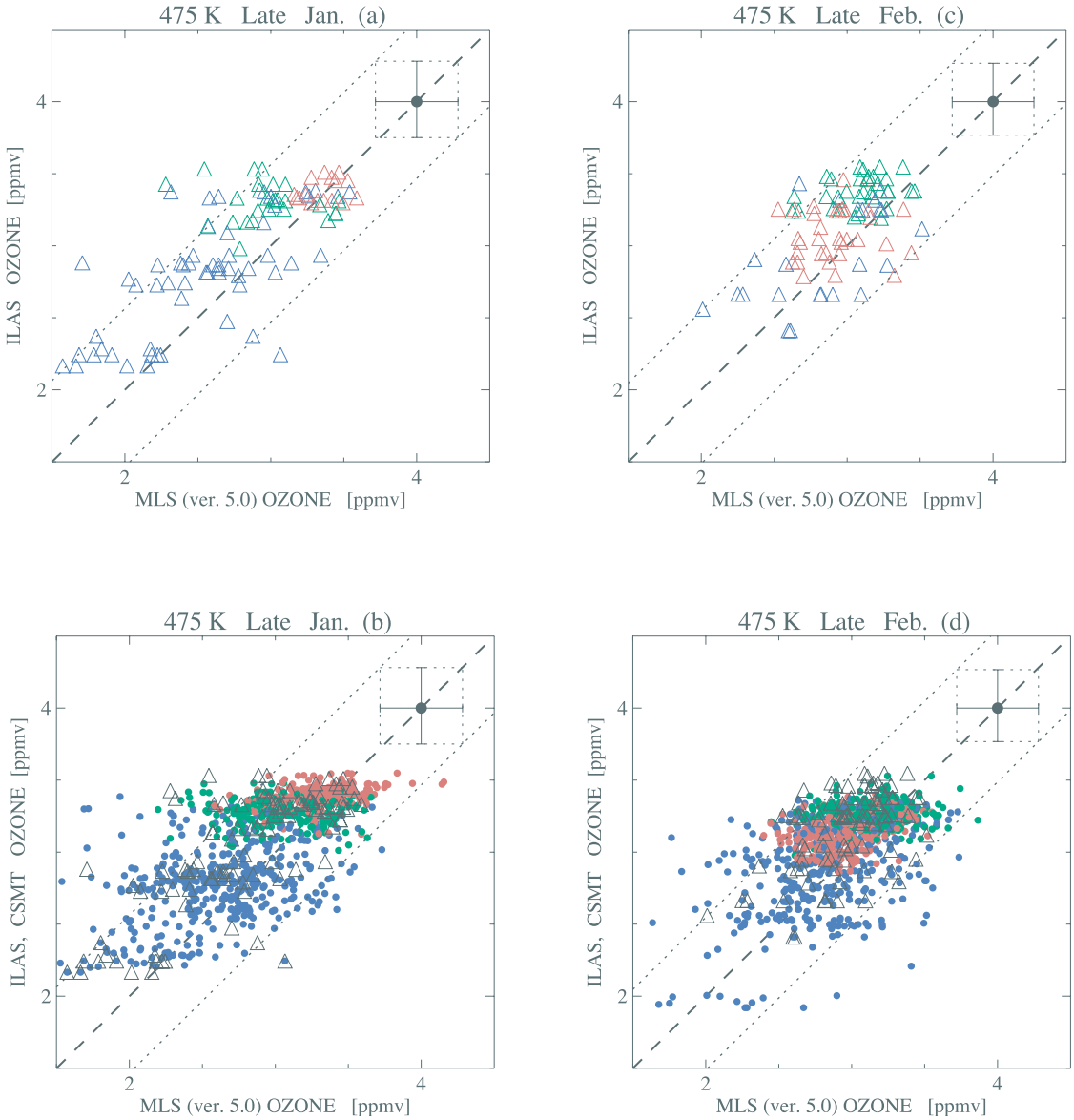

Figure 7. (a) Scatterplot of ILAS and MLS ozone for data on 28, 29, 31 January and 1 and 2 February at 475 K. Triangle points show the scatterplots for the original MLS and ILAS data within the criteria of 400 km and ±12 hours. Red, green, and blue dots indicate the data at the inside, boundary, and outside the vortex, respectively. Dashed line indicates one-to-one line, and error bars of ILAS or MLS data are also shown on the line with a solid circle. The errors are estimated by averaging ILAS or MLS errors in data. (b) Superimposition of CSMT ozone on Figure 7a. The colored dots show the scatterplots for MLS and CSMT data within the same criteria. The scatterplots of original MLS and ILAS data are also shown as black triangles. (c and d) As in Figures 7a and 7b but for data on 20, 21, 23, 24, and 26 February at 475 K.

Many of the radical species have no observational counterpart with which to compare, but ClO data are available from MLS.

[29] Validation of the version 3 ClO data from MLS was reported by *Waters et al.* [1996]. The accuracy and precision of version 4 MLS data at 46 hPa were 0.4 ppbv and 0.2 ppbv, respectively. Figure 11 shows CSMT ClO on 20 February; ClO data are plotted only in sunlit regions. Thick solid lines represent 10 hours (outer line) and 5 hours (inner line) of sunlight each day. The thin line indicates the vortex edge. The CSMT map shows ClO strongly activated in the polar vortex at around 120–135°E and

Table 5. Summary of the Comparison of MLS and CSMT-Derived Ozone Data

	Late January		Late February	
	ILAS	CSMT-Derived	ILAS	CSMT-Derived
Number of the data	101	852	88	909
Correlation coefficient	0.74	0.67	0.51	0.50
RMS, [a] %	15.22	11.24	9.86	9.17
Bias, [b] %	12.54	7.40	6.91	4.90

[a] $\mathrm{RMS} = 100 \times \frac{1}{N}\sum_{i=1}^{N}\frac{\sqrt{(\mathrm{ILAS}_i(\mathrm{CSMT}_i)-\mathrm{MLS}_i)^2}}{\mathrm{MLS}_i}$.

[b] $\mathrm{Bias}(\Delta) = 100 \times \frac{1}{N}\sum_{i=1}^{N}\frac{(\mathrm{ILAS}_i(\mathrm{CSMT}_i)-\mathrm{MLS}_i)}{\mathrm{MLS}_i}$.

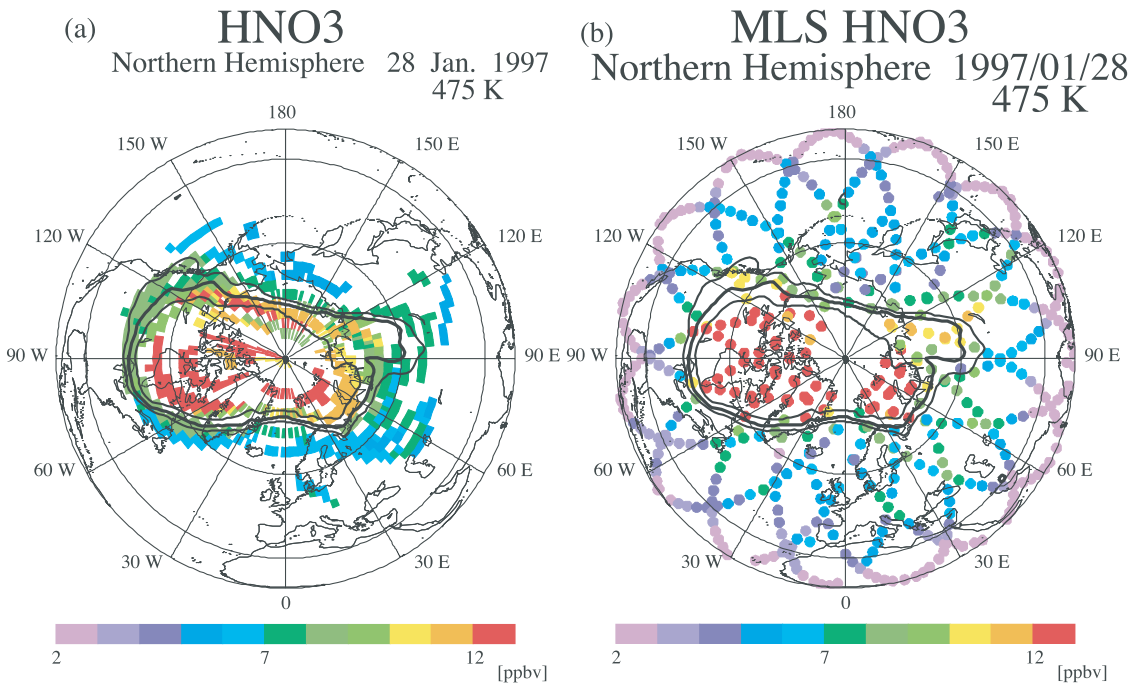

Figure 8. (a) Map of 475 K CSMT HNO_3 (ppbv) on 28 January 1997. (b) The 475 K MLS version 5 HNO_3 (ppbv) on 28 January 1997.

40–80°W at ~60°N; compare this to the version 4 ClO in the work of *Santee et al.* [1997, Figure 2] for the same day, with the same sunlit condition. Observation times must be adjusted to compare the ClO map from CSMT with that from MLS because ClO has a large diurnal variation. The two maps are nevertheless comparable, even without strict adjustment of the observation time because the sunlit area is limited to the same longitudes at a given time, and the sunlit regions for both CSMT and MLS are consistent. The ClO activation area as in the work of *Santee et al.* [1997, Figure 2] is consistent with the CSMT-derived ClO distribution, even though ClO activation in CSMT is less than MLS ClO. Part of the quantitative difference is due to the bias in MLS version 4 data. Version 5 of the MLS algorithm yields less ClO at 46 hPa than version 4 (Figure 11).

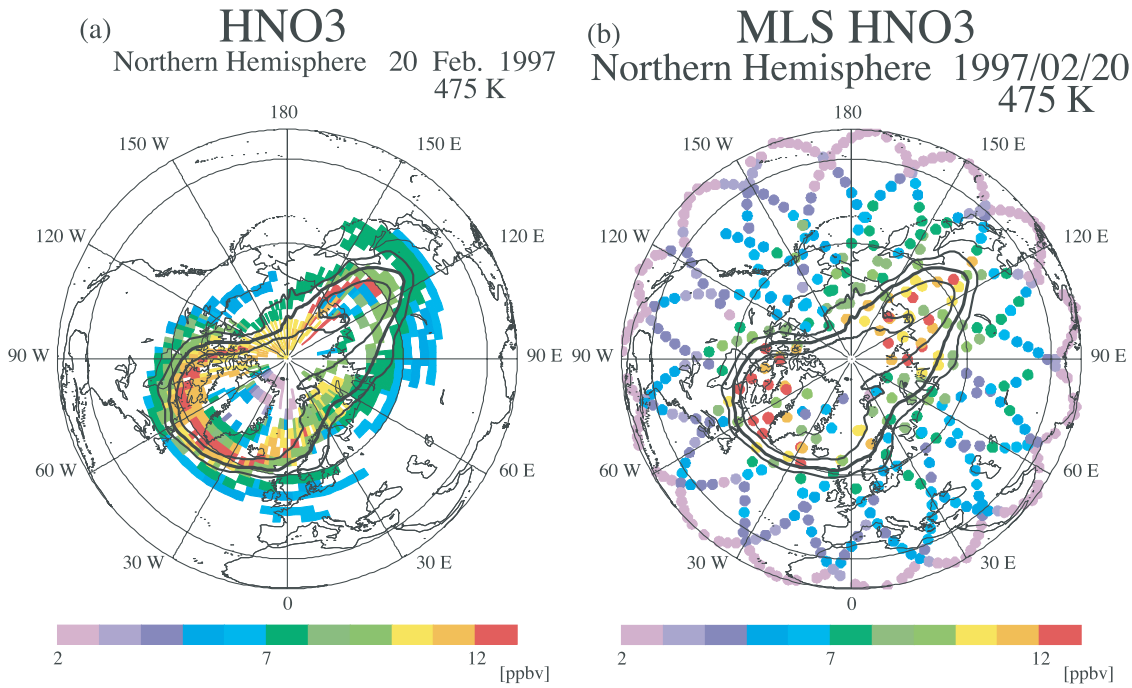

Figure 9. (a) As in Figure 8a but for 20 February. (b) As in Figure 8b but for 20 February.

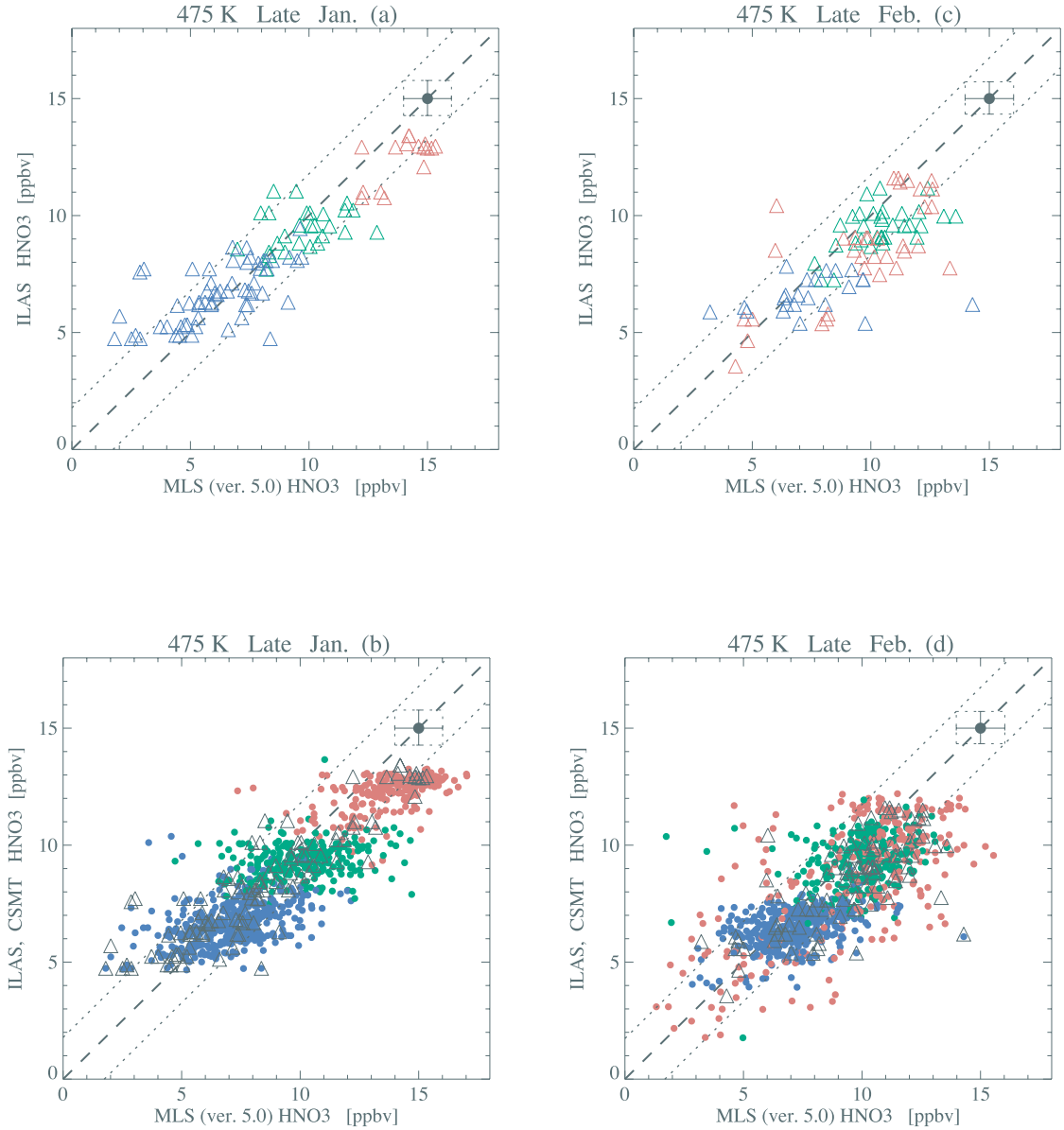

Figure 10. (a) Same as Figure 7 but for HNO_3. (b) Superimposition of MLS and CSMT HNO_3 on Figure 10a. (c and d) As in Figures 10a and 10b but for data on 20, 21, 23, 24, and 26 February.

[30] Because ClO has a large diurnal variation, a different approach for comparing MLS and CSMT ClO data in the same photochemical situation (same local time) was adopted. The time difference criteria for the comparison were greatly reduced, and the spatial criteria were relaxed. We selected 18 circles of 1000-km radius along 75°N latitude at 20° intervals to compare. The 75°N latitudinal band was chosen because most of the area falls inside the vortex. In addition, that latitude yields enough CSMT data for a valid comparison. All MLS data (usually about three) and CSMT data (typically six to seven) that fell within the 1000-km radius disk and had times that were within an hour of each other were averaged and compared. The criteria of an hour and 1000-km distance are similar to values used in a NO_2 validation study [*Irie et al.*, 2002].

[31] Figure 12 is a scatterplot for the ClO data. The accuracy and precision of version 5 of the MLS data at 46 hPa are estimated as 0.2 ppbv and 0.3 ppbv, respectively. Although CSMT values are somewhat smaller than MLS values, ClO_x activations at ~1.5 ppbv in CSMT are consistent quantitatively with those in simulations by a chemical transport model inside the vortex in late February 1997 at θ = 475 K [*Chipperfield and Pyle*, 1998]. Because a positive bias of 0.09 ppbv exists at 46 hPa in MLS version 5 ClO (MLS version 5 readme file), the one-to-one correlation line can be shifted to the right as shown by a solid line in the figure. Most of the data pairs are consistent with the solid line given the large MLS error range. This consistency between the two data sets verifies the reasonable ClO activation produced by the model. However, there is a still systematic underestimate in ClO derived from CSMT-scheme for the cases of high chlorine activation, which may cause less ozone destruction in the model than observed. *Danilin et al.* [2000] and *van den Broek et al.*

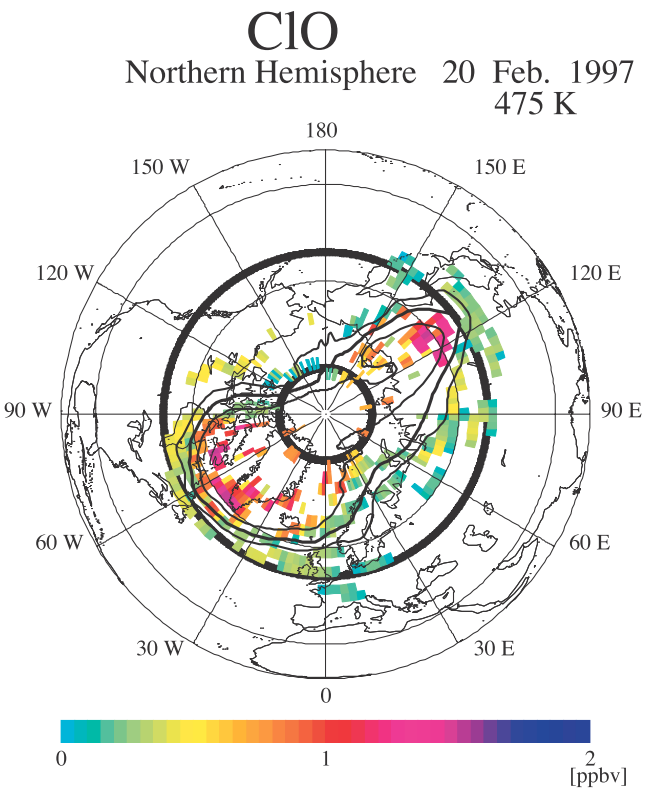

Figure 11. Map of 475 K CSMT ClO (ppbv) on 20 February 1997. Only data during sunlit hours were used for mapping. Thick solid lines indicate five hours and ten hours of sunlight in a day. The solid lines are the boundaries of the polar vortex as in Figure 5a.

[2000] also reported similar underestimation of ClO relative to MLS data. This issue is discussed in the next section again (Figure 12).

4. Discussion

4.1. Arctic Ozone in the Late Winter/Spring of 1997

[32] Because it controls photochemical processes, solar zenith angle, which is linked in a straightforward manner to geographical latitude and season, is treated carefully in the present study. The focus is the temporal evolution of chemical processes in the Arctic in the winter of 1997 as a function of changes in the solar zenith angle, rather than as a function of other dynamical parameters, such as equivalent latitudes or relative potential vorticity. Classification according to geographical latitude is not essentially different from that of equivalent latitudes for a symmetric polar vortex. The Arctic in the winter of 1997 was dominated by a strong symmetric vortex beginning in late February [*Coy et al.*, 1997] and persisting through early spring. Therefore geographical latitude in March 1997 was better correlated to relative location in the polar vortex than in other Arctic winters [*Guirlet et al.*, 2000]. In January 1997, however, the vortex deformed significantly, and parts of it were exposed to strong solar radiation that enhanced ClO levels in some areas.

[33] Figure 13 depicts the latitudinal coverage of air parcels that were advected from the ILAS measurement points. All initial points (ILAS measurements) were inside

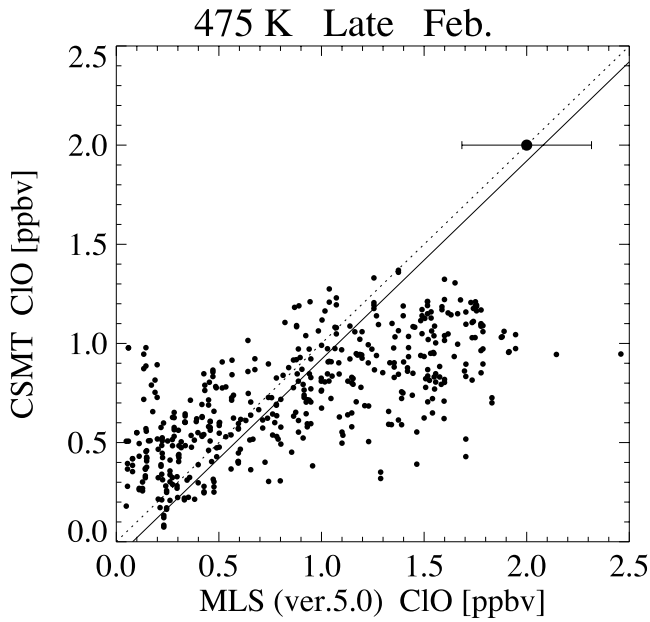

Figure 12. Scatterplot of MLS and CSMT ClO for the data on 20, 21, 23, 24, and 26 February at 475 K. Dotted line shows one-to-one correlation. Averaged error of MLS data is also shown. Solid line indicates one-to-one correlation after subtracting known bias value of 0.09 ppbv at 46 hPa in MLS version 5.

the inner edge of the vortex boundary. Dots in the figure are the daily averaged latitudes of air parcels. About 30–40 data points were available every day. Scatter of the dots in Figure 13 is restricted to between 85–55°N, reflecting the latitude range of ILAS measurements. The dots extend to lower latitudes near 50° in mid-January following the vortex distortion as noted above. Color indicates the minimum

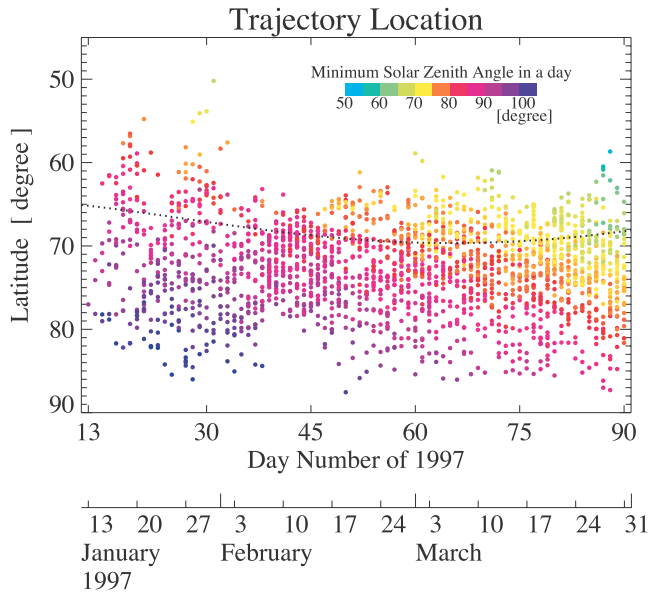

Figure 13. Latitudinal distribution of the air parcels for each day. Colored dots show the locations of air parcels on respective trajectories for each day. The minimum solar zenith angle each day is indicated with a color code. Black dots indicate the latitude of ILAS measurement points.

solar zenith angle experienced by an air parcel in a day. The continuous decrease in solar zenith angle after late February reflects the seasonal change (Figure 13).

[34] Figure 14 shows time series of the ozone mixing ratios calculated for the points in Figure 13. Dots depict the ozone mixing ratio at 475 K at 0000 UTC for each day as obtained from CSMT calculations with starting points inside the inner edge of the vortex boundary. Mean values, averaged for all data for every day, are connected with a solid line. The figure shows that the average ozone mixing ratio was nearly constant from January through mid-February before starting to decline in mid-February and then continuously decreasing until the end of March. There was considerable scatter in ozone mixing ratios in March, suggesting nonuniform ozone distribution in the polar vortex associated with chemical ozone changes and dynamical mixing (Figure 14).

4.2. Chemical Ozone Loss Rate From January Through March 1997

[35] Figure 15a shows time series of chemical ozone loss rates (ppbv/day) estimated from 24-hour differences in ozone mixing ratios along trajectories in the chemical box model. In contrast to the time variation of the ozone mixing ratios in Figure 14 that include dynamical effects, the ozone loss rates shown in Figure 15 are attributed to chemical change alone because they are determined from model calculations. Figure 15a is for a control run, assuming STS formation. As in Figure 13, color indicates the minimum solar zenith angle during the 24 hours of integration of each day for each trajectory. Daily mean values are shown

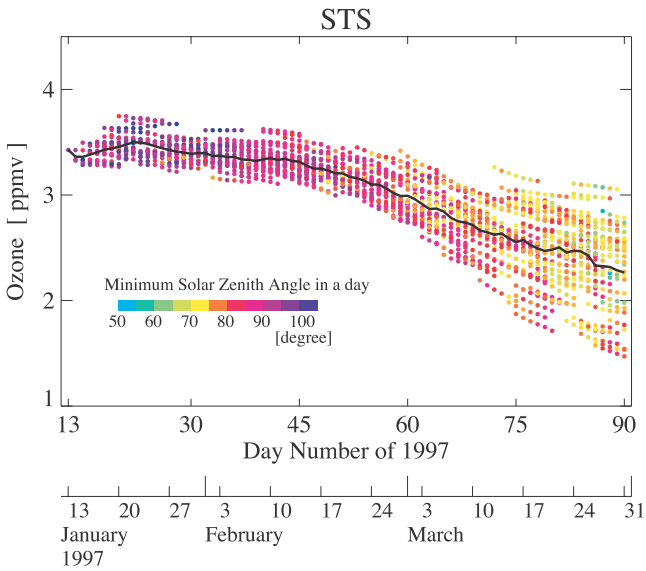

Figure 14. Time series of the calculated ozone by CSMT on 475 K at about 0000 UTC for each day. All of the initial points of trajectories (ILAS observation points) were taken inside the polar vortex. Information on the vortex edge was provided by ILAS/DHF, based on UKMO meteorological data using the approach of *Nash et al.* [1996]. Dots indicate the ozone-mixing ratios calculated for the target day along different trajectories. The color indicates the minimum value of the solar zenith angle experienced during each trajectory. The thick solid line is the average.

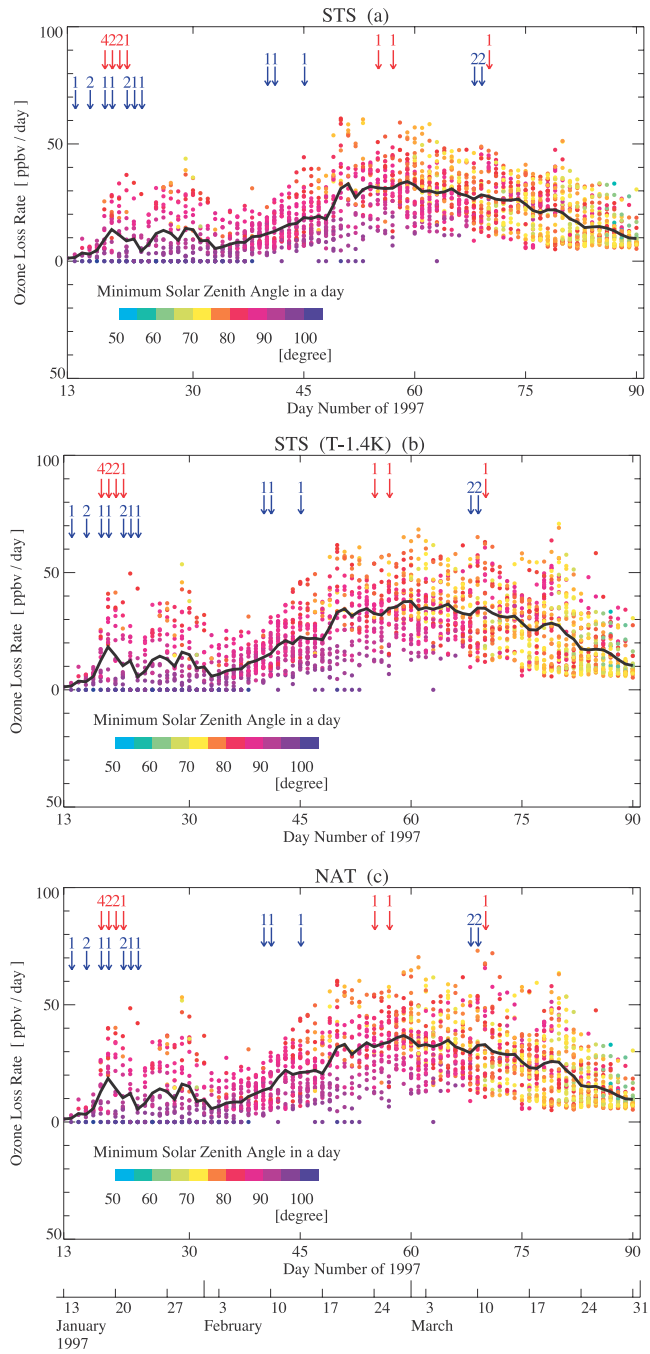

Figure 15. (a) Calculated ozone loss rates in ppbv/day for the STS case. Ozone decrease is taken to be positive. Each dot indicates the ozone loss rate calculated for the target day along different trajectories. Ozone loss was estimated from the difference between the first calculated output of the target day and the value 24 hours later. The color indicates the minimum value of the solar zenith angle experienced during each calculation. The thick solid line is the average. The numbers of STS (red) and NAT/NAD (blue) events observed at an altitude of 475 ± 25 K with ILAS [*Saitoh et al.*, 2002] are indicated in the figure. (b) Same as Figure 15a but for the lower temperature case. (c) Same as Figure 15a but for the NAT case.

by a solid line. The mean ozone loss rates were positive (ozone decreasing) throughout January, with small peaks on 19, 26, and 29 January. Mean ozone loss increased gradually toward late February, and exceeded 20 ppbv/day for 31 consecutive days. The maximum rate (black solid line) was 34 ± 10 (mean ± one-σ value) ppbv/day on 28 February. The mean ozone loss rate slowly decreased throughout March.

[36] *Knudsen* [1996] reported that ECMWF temperatures have a warm bias of about 1.4 K near 475 K. The effect of this warm bias for the case of STS formation is shown in Figure 15b. For these calculations, all temperatures are initially 1.4 K colder than the control run. As a result, as shown in the figure, ozone decreases more rapidly. The maximum loss is 38 ± 13 ppbv/day on 28 February. No significant difference in average ozone loss rates exists between the control run and the warm bias case. However, relatively large increases of ozone loss rates occur around 20 January and from early February to late March. Minimum temperatures along trajectories in this study are almost equivalent to minimum temperatures over the polar region as reported by *Chipperfield and Pyle* [1998, Plate 1]. The temperatures are between the STS formation temperature (~192 K) (T_{STS}) and 1.4 K higher ($T_{STS} < T < T_{STS+1.4\ K}$) from 15 to 25 January, from 5 February to 10 March, and from 17 to 20 March. The increase in the surface area due to STS formation is significant in those periods when the warm bias of 1.4 K is considered. Many of the reaction probabilities for heterogeneous reactions increase nonlinearly with temperature and are more sensitive to colder temperatures. Thus reaction probabilities increase when original temperatures are as low as those accompanying STS formation. The heterogeneous reaction rate is determined by the product of aerosol surface area and reaction probability (γ), so the increase in heterogeneous reactions rates is significant in the periods mentioned above, followed by an increase in ozone loss.

[37] Figure 15c shows the results if NAT formation is assumed instead of STS formation. The time series of ozone loss rate is similar to that in Figure 15a, although ozone decreases more for all periods. The maximum rate of ozone loss is 37 ± 11 ppbv/day on 28 February. The increased ozone loss rates for NAT do not differ significantly from those for STS, but the increases are relatively large in the second half of January and from early February to late March, similar to the warm bias case. Larger ozone loss rates in this case are linked to differences in PSC growth and reaction probabilities between NAT and STS. The temperature threshold of particle formation is about 3 K higher for NAT than for STS (around 195 K), and the enhancement of PSC surface area is significant. Although reaction probabilities (γ) for NAT for all heterogeneous reactions are not always larger than those of STS, resultant heterogeneous reaction rates for NAT are larger than those for STS. Therefore the ozone loss rates are again enhanced in those periods, as in the warm bias case.

[38] The numbers of STS (red) and NAT/NAD (blue) events observed with ILAS at an altitude of 475 ± 25 K are shown in Figures 15a–15c, which was adapted from *Saitoh et al.* [2002]. Some NAT/NAD events (blue) were observed in mid-January, mid-February, and mid-March. In these periods, the ozone loss rate would be larger than the loss in the control run. However, ozone loss rate does not depend significantly on PSC type, as shown in Figures 15a and 15c; the integrated ozone loss for NAT for all the periods is only 5% larger than that for STS case. PSC growth mechanisms are poorly understood, and many sophisticated PSC growth theories are now being investigated. Nevertheless, ozone losses calculated using the thermodynamic theory of PSC growth are reasonable in many simulations. Our estimated ozone loss rates are within an acceptable range, despite shortcomings in the PSC formation model (Figure 15).

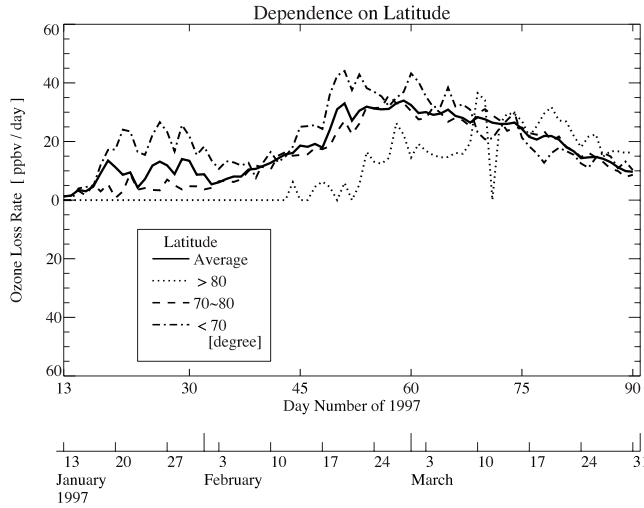

Figure 16. Dependence on latitude of the ozone loss rate in ppbv/day. The four lines are: (solid) averaged for all latitudes, (dotted) 80–90°N, (dashed) 70–80°N, and (dashed and dotted) latitudes equatorward of 70°N.

[39] As noted above, ozone loss rates are sensitive to solar radiation, so latitude or solar zenith angle must be considered when these results are compared to other studies. Figure 16 shows a clear latitudinal dependence in the rate of chemical ozone loss. Ozone loss occurred mainly at lower latitudes until late February. In March, the region of significant ozone loss shifted to higher latitudes, consistent with other studies [e.g., *Chipperfield and Pyle*, 1998] (Figure 16).

[40] Figure 17 shows the ratio of the integrated ozone loss relative to the initial ozone mixing ratio on 13 January, which is comparable to *Chipperfield and Pyle* [1998, Figure 1]. Integrated ozone loss was ~41% when averaged within the inner edge of the polar vortex. Integrated ozone loss amount depends on latitude as shown in Figure 16 because of inhomogeneities in ozone loss rates in the polar vortex. To explain chemical processes in ozone destruction, the time series of the representative partitioning (HCl, $ClONO_2$, and ClO_x (= Cl + ClO + $2Cl_2O_2$)) of total inorganic chlorine (Cl_y) for the control run are investigated. Mixing ratios of HCl and $ClONO_2$ decreased in late January and in late February as ClO_x increased, suggesting a conversion from inactive chlorine to active chlorine during those periods. The small enhancement of ClO_x that occurred in late January was affected by activation under relatively strong solar radiation at the edge of the vortex, when it deformed to lower latitudes after PSCs formed at low temperatures. The maximum ClO mixing ratio, about 1.6 ppbv, occurred in late February that corresponds to periods of significant chemical ozone depletion. Though

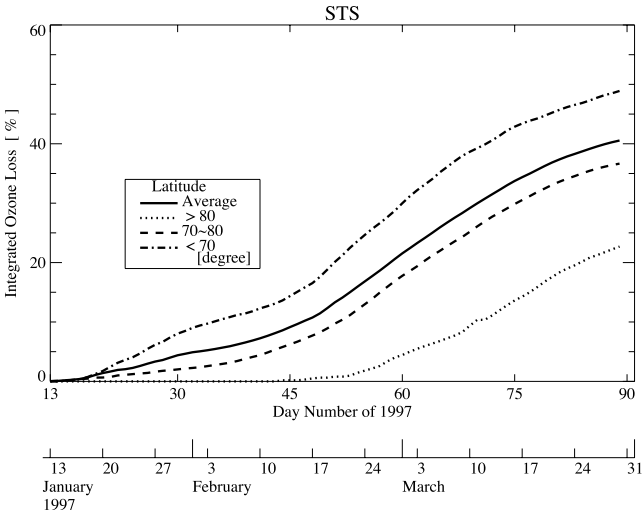

Figure 17. The rate of ozone loss as a relative percentage of the ozone-mixing ratio on 13 January 1997. The four lines are the same meaning with Figure 16.

this value is almost consistent with the estimate from other studies [e.g., *Rex et al.*, 2003], CSMT cannot reproduce high ozone loss in January nor high activation of ClO_x as discussed by *Rex et al.* [2003]. Here our analysis in based on only observed ozone and nitric acid, and no realistic amount of chlorine species is included. To improve the deficit in active chlorine, we need more information on observed chlorine species (Figure 17).

[41] Figure 18 shows the time series of the HNO_3 calculated by CSMT on 475 K at about 0000 UTC for each day, as done for ozone in Figure 14. Initial trajectory points lie inside the polar vortex. Dots indicate the HNO_3 mixing ratio calculated for the target day along different trajectories. The thick solid line depicts the daily mean, and color indicates the minimum SZA. Some HNO_3 measurements are significantly lower in late February. *Kondo et al.* [2000] and *Irie et al.* [2001] reported that denitrification started just after 10 February at altitudes of 17–21 km. *Irie et al.* [2001] calculated a significant denitrification (43%) from ILAS HNO_3 data at 19 km (near 475 K) in late February. Because the significant denitrification in late February would cause low mixing ratios of HNO_3 at θ = 475 K that would persist, the denitrification should have influenced ozone recovery in the spring of 1997 as a consequence of prolonged ClO_x activation. In our model, the calculations described above implicitly involve denitrification because denitrified gaseous HNO_3 data were used as initial values. However, the net effect of denitrification is difficult to determine because denitrification enhances Cl_y-catalyzed ozone loss but suppresses NO_x-catalyzed ozone loss. Analysis to distinguish the effect of denitrification is ongoing (Figure 18).

4.3. Estimate of the Effect With/Without Diabatic Cooling

[42] In the model calculations, "representative initial values" initialize the chemical species other than the observed species, as described in section 3.1. The data set of "representative initial values" were obtained from model calculations of 36 air parcels along "representative trajectories" for 90 days on the same isentropic surface, such as 475 K without diabatic descent. As reported by *Knudsen et al.* [1998], the air mass at 475 K on 10 April, 1997 was at 590 K on 1 January, 1997, and the effect of diabatic descent might have caused a significant error in the initial values, leading to a considerable bias in the calculated results. We estimated the amount of possible error in the calculated ozone loss rates. Calculations along diabatic descending trajectories as in the work of *Knudsen et al.* [1998, Figure 1] are very complicated because of the adjustments needed for pressure, temperature, air number density, and J-values. Here we use an alternative approach to estimate the error for representative initial values. We calculated "initial representative values" at 550 K, and applied them to CSMT calculations at 475 K, and the results were compared with the control run shown in Figure 15a. This error estimate will be the upper limit of the actual error, as trajectories should not remain at 550 K for 90 days. The ozone loss rates at 475 K obtained by incorporating initial values from 550 K were not different qualitatively from those in the control run: both show a continuous ozone decrease from January to March with a peak in late February. "Representative initial values" do not substantially influence the results because ozone and nitric acid (therefore NO_y) are constrained from measurements, and Cl_y and Br_y are fixed. Therefore possible errors in the results associated with the poorly determined initial values would not be large, even though the diabatic descent rate may be significant. In the present example, the integrated ozone loss at 475 K using initial values at 550 K from January to March is 25% lower than the ozone loss in the control run. However, the effect estimated here is the upper limit of the possible error. Nevertheless, quantitative estimates of the integrated ozone loss presented here must be carefully interpreted. Work to

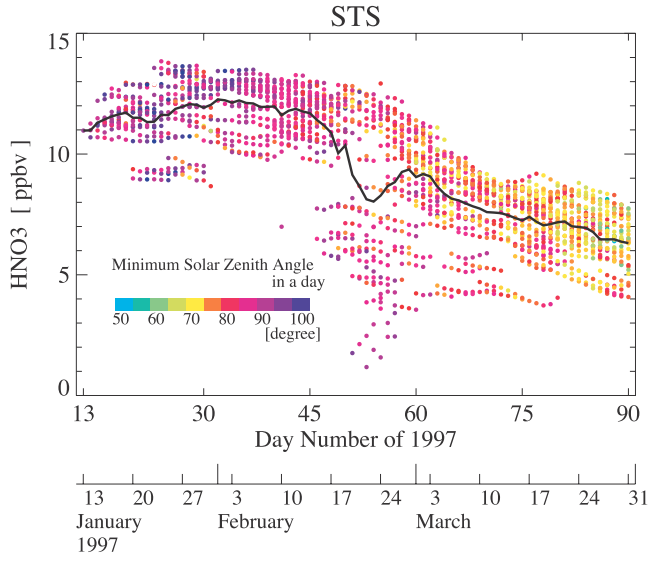

Figure 18. Time series of the calculated HNO_3 by CSMT on 475 K at about 0000 UTC for each day. All of the initial points of trajectories were inside the polar vortex, as in Figure 13. Dots indicate the HNO_3 mixing ratio calculated for the target day along different trajectories. The thick solid line depicts the average.

yield more realistic initial values is ongoing, and results will be reported in the near future.

4.4. Comparison With Other Studies

[43] In this section, present results are compared to other studies. Several studies used the SLIMCAT CTM to investigate the 1997 Arctic winter. *Chipperfield and Pyle* [1998] reported an ozone loss of 23% (relative to 1 January) in the Arctic winter of 1997 at 475 K for the area north of 60°N. *Hansen and Chipperfield* [1999] derived a similar ozone loss within the Arctic polar vortex at 475 K relative to 1 February. *Guirlet et al.* [2000] derived an ozone loss of 36% at 480 K north of 75°N equivalent latitude relative to 20 December 1996. Ozone loss rates depend on the location in the vortex as discussed above, so comparison of relative ozone loss amounts in various studies is not straightforward without a careful adjustment of the target region and the period. Nevertheless, our result is consistent with other studies based on SLIMCAT (compare Figure 15 with *Chipperfield and Pyle* [1998, Figure 1]), and an adjustment of the period decreases the difference between the studies. For example, the integrated ozone loss in the present study decreases to ~33% when the integration period is set from 1 February to 31 March to match more closely the values in the work of *Hansen and Chipperfield* [1999]. Furthermore, the continuous increase in the integrated ozone loss with the largest gradient in late February in this study (see Figure 15) is similar to features in the work of *Chipperfield and Pyle* [1998], *Hansen and Chipperfield* [1999], and *Guirlet et al.* [2000], suggesting the reliability of the simulations presented here.

[44] *Schulz et al.* [2000] derived a maximum ozone loss rate of ~40 ppbv/day at day number 60 in 1997 at 475 K inside the vortex, based on a ''Match'' analysis using sonde measurements. Chemical ozone loss rates estimated by Match inside the vortex in February are in good agreement quantitatively with our study. However, ozone loss rates in this study gradually decrease from late February to March, while ozone loss rates in the work of *Schulz et al.* [2000] drop from a high of ~40 ppbv in early March to a lower value in late March. This difference in ozone loss rates may reflect a change in the relative position in the polar vortex. The Match analysis in the second half of March does not represent the averaged condition in the polar vortex because only a few Match-pairs were taken at the vortex core [*Schulz et al.*, 2000]. Although the maximum ozone loss rates at day number ~60 by *Schulz et al.* [2000] are greater than values computed in this study for inside the vortex (~30 ± 12 ppbv/day), the two results do agree within 1-sigma value. *Manney et al.* [1997] estimated a chemical ozone loss rate of 1.3%/day using MLS data observed from 20 February through 26 February at 465 K, which corresponds to about 30 ppbv/day, consistent with estimates in this study of 30 ± 12 ppbv/day.

[45] As mentioned in the introduction, *Becker et al.* [1998, 2000] compared ozone loss derived from a Match analysis with that calculated using a chemical box model along the same trajectory as the Match pair in the Arctic winter and spring of 1992 and 1995. They found that the model underestimated ozone loss by Match in January, and suggested there should be an important unresolved issue in polar ozone chemistry. This issue is still being debated [e.g., *Rex et al.*, 2003]. Recently, *Terao et al.* [2002] applied Match techniques to ILAS data. They showed a maximum ozone loss of 60 ± 10 ppbv/day at 475 K in early March, a much larger loss than that in this study. However, their results cannot be interpreted as an overestimate of chemical ozone loss in measured data versus model predictions because Terao's estimate is even larger than the sonde-Match analysis by *Schulz et al.* [2000].

[46] To compare our estimate with the ozone loss derived by the Match technique based on ILAS measurement by *Terao et al.* [2002], we need to take several differences into account. First, Match analysis is more limited in spatial coverage than the results of this study because of the restricted selection of the Match-pairs. Another important point is the solar zenith angle observed on the trajectories. *Terao et al.* [2002] mentioned that differences in the SZA on the trajectories of satellite-Match and sonde-Match might produce a significant difference in the derived ozone loss amounts. *Rex et al.* [2003] also pointed out there may be some unresolved uncertainty in photodissociation efficiency for large solar zenith angle. Therefore comparison of the two results is not straightforward.

[47] The lower ozone destruction than Match analysis may be interpreted as underestimate of active chlorine in the model. Some model studies reported lower ClO than MLS ClO data [see *Danilin et al.*, 2000, Plate 3; *van den Broek et al.*, 2000, Plate 4]. To clarify this discrepancy, we need more observation of chlorine species. Fortunately, ILAS new version 6.0 of the algorithm succeeded to produce $ClONO_2$ recently. We are now pursuing a comparative study with the Match analysis group with $ClONO_2$ analysis, and results will appear in the near future.

5. Concluding Remarks

[48] The Chemical Species Mapping on Trajectories (CSMT) technique creates synoptic maps from asynoptic data by using a photochemical box model and trajectory analysis. Long and short lived species in the Arctic stratosphere were successfully mapped by CSMT. Initialization was achieved using ILAS ozone, HNO_3, and N_2O. CSMT-derived ozone data, which were compared to ozonesonde data; the CSMT scheme preserved the reliability of ozone data even after mapping. The CSMT-derived ozone, HNO_3, and ClO data were also compared with MLS version 5 data, showing good consistency between the two data sets. Such consistency supports the validity of the CSMT technique.

[49] The CSMT technique yields useful information about minor species where complicated chemical and/or dynamical processes occur, as in the Arctic because the spatial distributions of long- and short-lived chemical species can be presented on a global scale. The CSMT method can be categorized as a data-assimilation scheme. A characteristic of the technique is that chemical species are mapped on grids only where the data are constrained by observations. CSMT can be applied to any kind of data set. It can produce global maps when combined with satellite data with wide-coverage such as MLS. In this study, however, the coverage of CSMT maps was restricted to north of 60°N because of ILAS data limitations.

[50] CSMT showed significant chemical ozone loss in the late winter and spring of 1997 in the Arctic vortex. The maximum ozone loss rate was 34 ± 10 ppbv/day in late February, and the integrated ozone loss in the polar vortex

from 13 January to 31 March was 41%, averaged for the STS case. Ozone decreased more for all periods when the warm bias in the ECMWF temperatures was corrected. The maximum rate of mean ozone loss was 38 ± 13 ppbv/day in late February. If NAT are assumed rather than STS, similar losses occur: the maximum mean ozone loss was also 37 ± 11 ppbv/day in late February. Results are fairly consistent with chemical ozone losses reported in other studies of the same winter, which suggests that the model simulated the chemical ozone loss in this period reasonably well.

[51] Simultaneous observations by ILAS of ozone, HNO_3, H_2O, and PSCs at relatively high resolution allow a detailed discussion of ozone loss. Because the rate of ozone loss is sensitive to solar zenith angle, ozone loss significantly depends on latitude. Although ozone loss proceeded mainly at lower latitudes until late February in the polar vortex, the region of significant ozone loss shifted to higher latitudes in March. The chemical analysis in this study is still preliminary. A more detailed analysis in a future study including other minor species is possible.

Appendix A: Chemical Species Included in the Model

[52] $O(^1D)$, O, O_3H, OH, H_2, HO_2, H_2O, H_2O_2N, NO, NO_2, NO_3, N_2O, HNO_3, HO_2NO_2, N_2O_5Cl, ClO, Cl_2, OClO, ClOO, Cl_2O_2, HCl, HOCl, $ClONO_2Br$, BrO, HBr, HOBr, BrCl, $BrONO_2CH_4$, CHO, CH_2O, CH_3, CH_2, CH_3O, CH_3O_2, CH_3OOH, CO, CO_2CH_3Cl, CH_3BrCCl_4, CH_3CCl3, CFC11 (CCl_3F), CFC12 (CCl_2F_2), CFC13 ($CClF_3$)CFC113 (CCl_2FCClF_2), CFC114 ($CClF_2CClF_2$), CFC115 (CF_3CClF_2) HCFC22 ($CHClF_2$), HCFC141B (CH_3CCl_2F), HCFC142B (CH_3CClF_2) Halon1211 ($CBrClF_2$), Halon1301 ($CBrF_3$)N_2, O_2 (O_2 = 0.2095, N_2 = 0.7905 MR)

Appendix B

[53] Because radicals that destroy ozone are sensitive to sunlight, solar radiation should be computed precisely in models of the polar regions in winter and spring. Z_{sun}, the maximum solar zenith angle determining sunlit duration, is defined as:

$$Z_{sun} = \frac{\pi}{2} + \sqrt{\frac{2z}{a}}(\text{in radians}), \tag{B1}$$

where z is the altitude in km and a is Earth's radius (~6370 km). (When z = 20 km, Z_{sun} is about 94°.)

[54] For solar zenith angles (θ) from 0 to 75°, air mass factors (f) that determine the attenuation of solar radiation are defined by

$$F = \sec\theta. \tag{B2}$$

From 75° to 90°, the formula of the Garcia-Solomon model [*Solomon et al.*, 1985] was used:

$$F = \frac{35}{\sqrt{1224\ \cos^2\theta + 1}}. \tag{B3}$$

[55] The Chapman function was used for $90° < \theta < Z_{sun}$ [*Brasseur and Solomon*, 1984]:

$$F = \sqrt{\frac{\pi x}{2}\sin\theta}\left\{1 + erf\left(-\cot\theta\sqrt{\frac{x\sin\theta}{2}}\right)\right\}\left(1 + \frac{3}{8x\ \sin\theta}\right), \tag{B4}$$

where $\text{erf}(x) = \frac{2}{\sqrt{\pi}}\int_0^x e^{-\xi^2}d\xi$, $x = (a + z)/h$, and h is the scale height (~7 km).

[56] **Acknowledgments.** We are grateful to Jean-François Lamarque and Stacy Walters of the Atmospheric Chemistry Division, NCAR, for providing the preprocessor. The authors thank Susan Solomon for making her model available, and Sachiko Kawase, Nara Women's University, for helping to develop CSMT. Thanks also to Naoko Saitoh, Nara Women's University for providing PSC data by ILAS. This research used EORC-TAM, a trajectory calculation tool developed by the Earth Observation Research Center of NASDA. ILAS data were provided by ILAS/DHF at NIES, and we would like to express our gratitude to Yasuhiro Sasano and all members of the ILAS science team.

References

Becker, B., R. Müller, D. S. Mckenna, M. Rex, K. S. Carslaw, and H. Oelhaf, Ozone loss in the Arctic stratosphere in the winter 1994/95: Model underestimate results of the Match analysis, *J. Geophys. Res.*, *105*, 15,175–15,184, 2000.

Becker, G., R. Müller, D. S. Mckenna, M. Rex, and K. S. Carslaw, Ozone loss rate in the Arctic stratosphere in the winter 1991/92: Model calculations compared with Match results, *Geophys. Res. Lett.*, *25*, 4325–4328, 1998.

Bloss, W. J., S. L. Nickolaisen, R. J. Salawitch, R. R. Friedl, and S. P. Sander, Kinetics of the ClO self-reaction and 210 nm absorption cross section of the ClO dimer, *J. Phys. Chem. A*, *105*, 11,226–11,239, 2001.

Brasseur, G., and S. Solomon, *Aeronomy of the Middle Atmosphere*, D. Reidel, Norwell, Mass., 1984.

Brasseur, G. P., X. Tie, P. J. Rasch, and F. Lefevre, A three-dimensional simulation of the Antarctic ozone hole: Impact of anthrogenic chlorine on the lower stratosphere and upper troposphere, *J. Geophys. Res.*, *102*, 8909–8930, 1997.

Carslaw, K. S., S. L. Clegg, and P. Brimblecombe, A thermodynamic model of the system HCL-HNO_3-H_2SO_4-H_2O, including solubilities of HBr, from <200 to 328 K, *J. Phys. Chem.*, *99*, 11,557–11,574, 1995.

Chipperfield, M. P., and J. A. Pyle, Model sensitivity studies of Arctic ozone depletion, *J. Geophys. Res.*, *103*, 28,389–28,403, 1998.

Coy, L., E. R. Nash, and P. A. Newman, Meteorology of the polar vortex: Spring 1997, *Geophys. Res. Lett.*, *24*, 2693–2696, 1997.

Danilin, M. Y., M. L. Santee, J. M. Rodriguez, M. K. W. Ko, J. M. Mergenthaler, J. B. Kumer, A. Tabazadeh, and N. J. Livesey, Trajectory hunting: A case study of rapid chlorine activation in December 1992 as seen by UARS, *J. Geophys. Res.*, *105*, 4003–4018, 2000.

Danilin, M. Y., et al., Trajectory hunting as an effective technique to validate multiplatform measurements: Analysis of the MLS, HALOE, SAGE-II, ILAS, and POAM-II data in October–November 1996, *J. Geophys. Res.*, *107*(D20), 4420, doi:10.1029/2001JD002012, 2002.

DeMore, W. B., D. M. Golden, R. F. Hampson, C. J. Howard, M. J. Kurylo, M. J. Molina, A. R. Ravishankara, and S. P. Sander, Chemical kinetics and photochemical data for use in stratospheric modeling, *Eval. 11, JPL Publ. 94-26*, Jet Propul. Lab., Pasadena, Calif., 1994.

DeMore, W. B., S. P. Sander, D. M. Golden, R. F. Hampson, M. J. Kurylo, C. J. Howard, A. R. Ravishankara, C. E. Kolb, and M. J. Molina, Chemical kinetic and photochemical data for use in stratospheric modeling, *Rep. 12*, Jet Propul. Lab., Pasadena, Calif., 1997.

Deshler, T., B. Nardi, A. Adriani, F. Cairo, G. Hansen, F. Fierli, A. Hauchecorne, and L. Pulvirenti, Determining the index of refraction of polar stratospheric clouds above Andoya (69°N) by combining size-resolved concentration and optical scattering measurements, *J. Geophys. Res.*, *105*, 3943–3953, 2000.

Dye, J. E., D. Baumgardner, B. W. Gandrud, S. R. Kawa, K. K. Kelly, M. Loewenstein, G. V. Ferry, K. R. Chan, and B. L. Gary, Particle size distributions in Arctic polar stratospheric clouds, growth and freezing of sulfuric acid droplets, and implications for cloud formation, *J. Geophys. Res.*, *97*, 8015–8034, 1992.

Fahey, D. W., et al., The detection of large HNO3-containing particles in the winter Arctic stratosphere, *Science*, *291*, 1026–1031, 2001.

Gao, R. S., et al., A comparison of observations and model simulations of NOx/NOy in the lower stratosphere, *Geophys. Res. Lett.*, *26*(8), 1153–1156, 1999.

Guirlet, M., M. P. Chipperfield, J. A. Pyle, G. Goutail, J. P. Pommereau, and E. Kyro, Modeled Arctic ozone depletion in winter 1997/1998 and comparison with previous winter, *J. Geophys. Res.*, *105*, 22,185–22,200, 2000.

Haggard, K. V., E. E. Ramsberg, W. L. Grose, J. M. Russell III, B. T. Marshall, and G. Lingenfelser, Description of data on the Nimbus 7 LIMS map arcival tape. Temperature and geopotential height, *NASA Tech. Rep., 2553*, NASA, Greenbelt, Md., 1986.

Hansen, G., and M. P. Chipperfield, Ozone depletion at the edge of the Arctic polar vortex 1996/97, *J. Geophys. Res.*, *104*, 1837–1845, 1999.

Hanson, D., Reaction of $ClONO_2$ with H_2O and HCl in sulfuric acid and $HNO_3/H_2SO_4/H_2O$ mixtures, *J. Phys. Chem. A*, *102*, 4794–4807, 1998.

Hanson, D., and K. Mauersberger, Vapor pressures of HNO_3/H_2O solution at low temperatures, *J. Phys. Chem.*, *92*, 6167–6170, 1988.

Hayashida, S., N. Saitoh, A. Kagawa, T. Yokota, M. Suzuki, H. Nakajima, and Y. Sasano, Arctic polar stratospheric clouds observed with the Improved Limb Atmospheric Spectrometer during winter 1996/97, *J. Geophys. Res.*, *105*, 24,715–24,730, 2000a.

Hayashida, S., N. Saitoh, M. Horikawa, Y. Amemiya, M. Hayashi, and Y. Sasano, Stratospheric background aerosols and polar stratospheric clouds observed with satellite sensors—Inference of particle composition and sulfate amount, *Soc. Photo. Opt. Instrum.*, 76–86, 2000b.

Hofmann, D. J., and J. M. Rosen, On the temporal variation of stratospheric aerosol size and mass during the first 18 months following the 1982 eruptions of El Chichon, *J. Geophys. Res.*, *89*, 4883–4890, 1984.

Irie, H., M. Koike, Y. Kondo, G. E. Bodecer, M. Y. Danilin, and Y. Sasano, Redistribution of nitric acid in the Arctic lower stratosphere during the winter of 1996–97, *J. Geophys. Res.*, *106*, 23,139–23,150, 2001.

Irie, H., et al., Validation of NO_2 and HNO_3 measurements from the Improved Limb Atmospheric Spectrometer (ILAS) with the version 5.20 retrieval algorithm, *J. Geophys. Res.*, *107*(D24), 8206, doi:10.1029/2001JD001304, 2002.

Kanzawa, H., M. Shiotani, M. Suzuki, T. Yokota, and Y. Sasano, Structure of the polar vortex of the Arctic winter of 1996/1997 as analyzed from long-lived tracer data of ILAS and meteorological data, in *Proceedings of the Quadrennial Ozone Symposium*, pp. 253–254, Natl. Space Dev. Ag. of Jpn., Tokyo, 2000.

Knudsen, B. M., Accuracy of Arctic stratospheric temperature analyses and the implications for the prediction of polar stratospheric clouds, *Geophys. Res. Lett.*, *23*, 3747–3750, 1996.

Knudsen, B. M., et al., Ozone depletion in and below the Arctic vortex for 1997, *Geophys. Res. Lett.*, *25*, 627–630, 1998.

Koike, M., et al., A comparison of Atctic HNO3 profiles measured by the Improved Limb Atmospheric Spectrometer and balloon-borne sensors, *J. Geophys. Res.*, *105*, 6761–6771, 2000.

Kondo, Y., H. Irie, M. Koike, and G. E. Bodeker, Denitrification and nitrification in the Arctic stratosphere during the winter of 1996–1997, *Geophys. Res. Lett.*, *27*, 337–340, 2000.

Lary, D. J., M. P. Chipperfield, R. Toumi, and T. Lenton, Gas phase atmospheric bromine photochemistry, *J. Geophys. Res.*, *101*, 1505–1516, 1996.

Lefevre, F., F. Figarol, K. S. Carslaw, and T. Peter, The 1997 Arctic ozone depletion quantified from three-dimensional model simulations, *Geophys. Res. Lett.*, *25*, 2425–2428, 1998.

Manney, G. L., et al., Chemical depletion of ozone in the Arctic lower stratosphere during winter 1992–93, *Nature*, *370*, 429–434, 1994.

Manney, G. L., L. Froidevaux, M. L. Santee, R. W. Zurek, and J. W. Waters, MLS observations of Arctic ozone loss in 1996–97, *Geophys. Res. Lett.*, *24*, 2697–2700, 1997.

Matsuzono, T., T. Sano, and T. Ogawa, Development of the Trajectory Analysis Model (EORC-TAM), *EORC Tech. Rep.*, Natl. Space Dev. Ag. of Jpn., Tokyo, 1998.

Morris, G. A., et al., Trajectory mapping and application to data from the Upper Atmosphere Research Satellite, *J. Geophys. Res.*, *100*, 16,491–16,505, 1995.

Morris, G. A., J. F. Gleason, J. Ziemke, and M. R. Schoeberl, Trajectory Mapping: A tool for validation of trace gas observations, *J. Geophys. Res.*, *105*, 17,825–17,894, 2000.

Müller, R., J. U. Groob, D. S. McKenna, P. J. Crutzen, C. Bruhl, J. M. Russell III, and A. F. Tuck, HALOE observations of the vertical structure of chemical ozone depletion in the Arctic vortex during winter and early spring 1996–1997, *Geophys. Res. Lett.*, *24*, 2717–2720, 1997.

Nash, E. R., P. A. Newman, J. E. Rosenfield, and M. R. Schoeberl, An objective determination of the polar vortex using Ertel's potential vorticity, *J. Geophys. Res.*, *101*, 9471–9478, 1996.

Newman, P. A., J. F. Gleason, R. D. McPeters, and R. S. Stolarski, Anomalously low ozone over the Arctic, *Geophys. Res. Lett.*, *24*, 2689–2692, 1997.

Pan, L. L., W. J. Randel, H. Nakajima, S. T. Massie, H. Kanzawa, Y. Sasano, T. Yokota, T. Sugita, S. Hayashida, and S. Oshchepkov, Satellite observation of dehydration in the Arctic polar stratosphere, *Geophys. Res. Lett.*, *29*(8), 1184, doi:10.1029/2001GL014147, 2002.

Pierce, R. B., W. L. Grose, J. M. Russell III, and A. F. Tuck, Evolution of Southern Hemisphere spring air mass observed by HALOE, *Geophys. Res. Lett.*, *21*, 213–216, 1994.

Portmann, R. W., S. Solomon, R. R. Garcia, L. W. Thomason, L. R. Poole, and M. P. McCormick, Role of aerosol variations in anthropogenic ozone depletion in the polar regions, *J. Geophys. Res.*, *101*, 22,991–23,006, 1996.

Rex, M., et al., Chemical ozone loss in the Arctic winter 1994/95 as determined by the match technique, *J. Atmos. Chem.*, *32*, 35–59, 1999.

Rex, M., R. J. Salawitch, M. L. Santee, J. W. Waters, K. Hoppel, and R. Bevilacqua, On the unexplained stratospheric ozone loss during cold Arctic Januaries, *Geophys. Res. Lett.*, *30*(1), 1008, doi:10.1029/2002GL016008, 2003.

Saitoh, N., S. Hayashida, L. L. Pan, and Y. Sasano, Characteristics of Arctic polar stratospheric clouds in the winter of 1996/97 inferred from ILAS measurements, *J. Geophys. Res.*, *107*(D24), 8205, doi:10.1029/2001JD000595, 2002.

Salby, M. L., Sampling theory for asynoptic satellite observations, I: Space-time spectra, resolution, and aliasing, *J. Atmos. Sci.*, *39*, 2577–2600, 1982a.

Salby, M. L., Sampling theory for asynoptic satellite observations, II: Fast Fourier synoptic mapping, *J. Atmos. Sci.*, *39*, 2601–2614, 1982b.

Salcedo, D., T. Luisa, and M. J. Molina, Homogeneous freezing of concentrated aqueous acid solutions at polar stratospheric temperatures, *J. Phys. Chem. A*, *105*, 1433–1439, 2001.

Sander, S. P., et al., Chemical kinetics and photochemical data for use in stratospheric modeling, *Rep. 13*, Jet Propul. Lab., Pasadena, Calif., 2000.

Sandu, A., J. G. Verwer, M. Vanloon, G. R. Carmichael, F. A. Potra, D. Dabdub, and J. H. Seinfeld, Benchmarking stiff ode solvers for atmospheric chemistry problems-I. Implicit vs. explicit, *Atmos. Environ.*, *31*, 3151–3166, 1997a.

Sandu, A., J. G. Verwer, J. G. Blom, E. J. Spee, G. R. Carmicheael, and F. A. Potra, Benchmarking stiff ode solvers for atmospheric chemistry problems II: Rosenbrock solvers, *Atmos. Environ.*, *31*, 3459–3472, 1997b.

Santee, M. L., G. L. Manney, L. Froidevaux, R. W. Zurek, and J. W. Waters, MLS observations of ClO and HNO_3 in the 1996–97 Arctic polar vortex, *Geophys. Res. Lett.*, *24*, 2713–2716, 1997.

Sasano, Y., M. Suzuki, T. Yokota, and H. Kanzawa, Improved Limb Atmospheric Spectrometer (ILAS) for stratospheric ozone layer measurements by solar occultation technique, *Geophys. Res. Lett.*, *26*, 197–200, 1999.

Sasano, Y., Y. Terao, H. L. Tnanaka, T. Yasunari, H. Kanzawa, H. Nakajima, T. Yokota, H. Nakane, S. Hayashida, and N. Saitoh, ILAS observations of chemical ozone loss in the Arctic vortex during early spring of 1997, *J. Geophys. Res.*, *27*, 213–216, 2000.

Schoeberl, M. R., H. MacLean, R. Swinbank, A. O'Neill, and F. W. Taylor, Reconstruction of the constituent distribution and trends in the Antarctic polar vortex from ER-2 flight, *J. Geophys. Res.*, *94*, 16,815–16,845, 1989.

Schulz, A., et al., Match observations in the Arctic winter 1996/97: High stratospheric ozone loss rates correlated with low temperature deep inside the polar vortex, *Geophys. Res. Lett.*, *27*, 205–208, 2000.

Sinnhuber, B. M., J. Langer, U. Klein, U. Raffalski, K. Kunzi, and O. Schrems, Ground based millometer-wave observations of Arctic ozone depletion during winter and spring of 1996/97, *Geophys. Res. Lett.*, *25*, 3227–3330, 1998.

Solomon, S., R. R. Garcia, and F. Stordal, Transport processes and ozone peturbations, *J. Geophys. Res.*, *90*, 12,981–12,989, 1985.

Sugita, T., et al., Validation of ozone measurements from the Improved Limb Stratospheric Spectrometer (ILAS), *J. Geophys. Res.*, *107*(D24), 8212, doi:10.1029/2001JD000602, 2002.

Terao, Y., Y. Sasano, H. Nakajima, H. L. Tanaka, and T. Yasunari, Stratospheric ozone loss in the 1996/1997 Arctic winter: Evaluation based on multiple trajectory analysis for double-sounded air parcels by ILAS, *J. Geophys. Res.*, *107*(D24), 8210, doi:10.1029/2001JD000615, 1997.

Tolbert, M. A., Sulfate aerosols and polar stratospheric cloud formation, *Science*, *264*, 527–528, 1994.

Tolbert, M. A., Polar clouds and sulfate aerosols, *Science*, *272*, 1597, 1996.

van den Broek, M. M. P., A. Bregman, and J. Lelieveld, Model study of stratospheric chlorine activation and ozone loss during the 1996/97 winter, *J. Geophys. Res.*, *105*, 29,961–28,978, 2000.

Warren, R., T. Gierczak, and A. R. Ravishankara, A study of O(1D) reactions with CFC substitutes, *Chem. Phys. Lett.*, *183*, 403–409, 1991.

Waters, J. W., et al., Validation of UARS Microwave Limb Sounder ClO measurements, *J. Geophys. Res.*, *101*, 10,091–10,127, 1996.

World Meteorological Organization (WMO), *Scientific Assessment of Ozone Depletion: 1998*, Geneva, 1999.

Yokota, T., H. Hakajima, T. Sugita, H. Tsubaki, Y. Itou, M. Kaji, M. Suzuki, H. Kanzawa, J. H. Park, and Y. Sasano, Improved Limb Atmospheric Spectrometer (ILAS) data retrieval algorithm for Version 5.20 gas profile products, *J. Geophys. Res.*, *107*(D24), 8216, doi:10.1029/2001JD000628, 2002.

S. Hayashida, Faculty of Science, Nara Women's University, Kita-uoya Nishi-machi, Nara 630-8506, Japan. (sachiko@ics.nara-wu.ac.jp)

A. Kagawa, Fujitsu FIP Corporation, Time 24 Building, 2-45, Aomi, Koto-ku, Tokyo 135-8686, Japan. (a.kagawa@fip.fujitsu.com)